TaO_x electron transport layers for CO_2 reduction Si photocathodes

Rajiv Ramanujam Prabhakar,[a,b,#] Raphaël Lemerle,[a,b,c,#] Magda Barecka,[d,e,f] Minki Kim,[a,b,g] Sehun Seo[a,b], Elif Nur Dayi,[a,b,c] Irene Dei Tos,[a,b] and Joel W. Ager,[a,b,h,i,]*

[a]Liquid Sunlight Alliance, Lawrence Berkeley National Laboratory, Berkeley, California 94720, United States

[b]Chemical Sciences Division, Lawrence Berkeley National Laboratory, Berkeley, California 94720, United States

[c]Materials Science and Engineering, École Polytechnique Fédéral de Lausanne, Lausanne 1015, Switzerland

[d]Department of Chemical Engineering, Northeastern University, 360 Huntington Avenue, 02215 Boston, USA; email: m.barecka@northeastern.edu

[e]Department of Chemistry and Chemical Biology, Northeastern University, 360 Huntington Avenue, 02215 Boston, USA

[f]Cambridge Centre for Advanced Research and Education in Singapore, CARES Ltd., 1 CREATE Way, CREATE Tower #05-05, 138602, Singapore.

[g]Chemical and Biomolecular Engineering, Korea Advanced Institute of Science and Technology (KAIST), Daejeon 34141, Republic of Korea

[h]Department of Materials Science and Engineering, University of California, Berkeley, Berkeley, CA 94720, USA

[i]Materials Sciences Division, Lawrence Berkeley National Laboratory, Berkeley, California 94720, United States

AUTHOR INFORMATION

# These authors contributed equally

Corresponding Author

[*]jwager@lbl.gov (J. W. Ager)

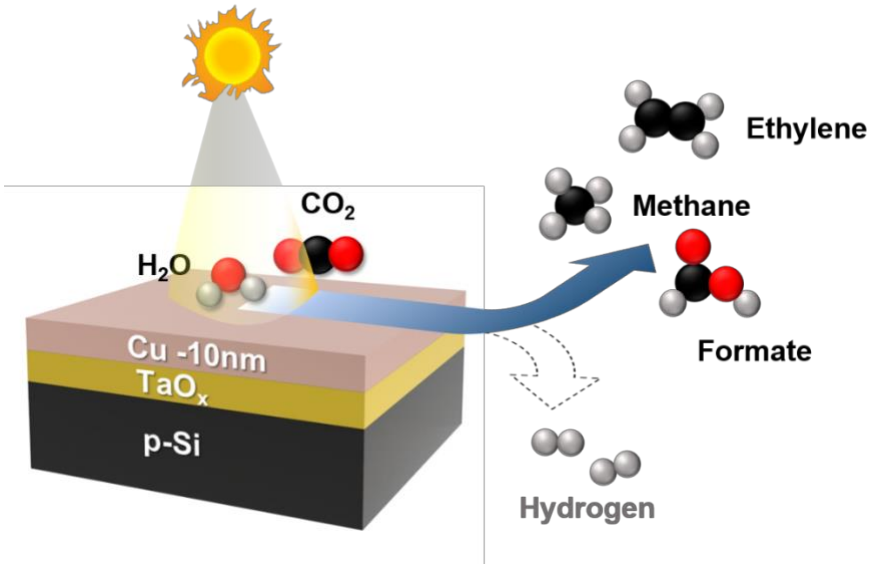

ABSTRACT

Electron transport layers (ETLs) used as components of photocathodes for light-driven CO_2 reduction (CO_2R) in aqueous media should have good electronic transport, be stable under CO_2R conditions, and, ideally, be catalytically inert for the competing hydrogen evolution reaction (HER). Here, using planar p-Si (100) as the absorbing material, we show that TaO_x satisfies all three of the above criteria. TaO_x films were synthesized by both pulsed laser deposition (PLD) and radio-frequency (RF) sputtering. In both cases, careful control of the oxygen partial pressure during growth was required to produce ETLs with acceptable electron conductivity. p-Si/TaO_x photocathodes were interfaced with ca. 10 nm of a CO_2R catalyst: Cu or Au. Under front illumination with simulated AM 1.5G in CO_2-saturated bicarbonate buffer, we observed, for both metals, faradaic efficiencies for CO_2R products of ~50% and ~30% for PLD TaO_x and RF sputtered TaO_x, respectively, at photocurrent densities up to 8 mA cm^{-2}. p-Si/TiO_2/Cu photocathodes were also evaluated but produced mostly H_2 (>97%) due to reduction of the TiO_2 to Ti metal under CO_2R

conditions. In contrast, a dual ETL photocathode (p-Si/TiO_2/TaO_x/Cu) was selective for CO_2R, which suggests a strategy for separately optimizing selective charge collection and the stability of the ETL/water interface. The maximum photovoltage obtained with p-Si/TaO_x/Cu devices was 300 mV which was increased to 430-460 mV by employing ion implantation to make pn^+-SiTaO_x/Cu structures. Photocathodes with RF sputtered TaO_x ETLs are stable for CO_2R for at least 300 min. Techno-economic analysis shows that the reported system, if scaled, could allow for an economically viable production of feedstocks for chemical synthesis under the adoption of specific CO_2 credit schemes, thus becoming a significant component to carbon-neutral manufacturing.

INTRODUCTION

Charge selective contacts (CSC) provide the asymmetric necessary for light to electrical power conversion in photovoltaic (PV) solar cells.[1] For this reason, in silicon PV there is significant research focus and progress on engineering CSCs that provide both efficient charge collection and interface passivation.[2–5] Energy conversion with photoelectrochemical (PEC) devices operates on the same principle: the surfaces of photocathodes must be selective for electrons and the surface of photoanodes must be selective for holes. While some materials, notably metal oxides used as photoanodes for the oxygen evolution reaction (OER), provide charge selectivity via their intrinsic catalytic activity for the desired reaction, engineered surface layers are also widely employed.[6,7]

For PEC electrodes, in addition to charge carrier selectivity, there are two additional constraints for CSCs. Firstly, the CSC must be stable in the electrochemical environment (often either strong base or acid) so that it can serve as a “protection” layer for the photoabsorber if it is a kinetically or thermodynamically unstable material during operation.[8] Further, the CSC either by itself or in combination with a co-catalyst must provide selectivity to the desired reaction, for instance

hydrogen evolution reaction (HER), oxygen evolution reaction (OER) or CO_2 reduction (CO_2R). Additionally, for the case of PEC CO_2R, since both HER and CO_2R are thermodynamically possible, the CSC or, more specifically, the electron transport layer (ETL) in combination with a co-catalyst must be selective to CO_2R products rather than HER.

There are numerous experimental reports which utilize a Si/ETL/co-catalyst stack to form photocathodes for HER.[9–11] TiO_2 and either Pt or Ru are typical choices for the ETL and HER catalyst, respectively. To make a photocathode which will instead reduce CO_2, the co-catalyst should be replaced with a metal which is more active for CO_2R than for HER.[12,13] For instance, Au has been reported to drive CO_2R more selectively towards CO,[14] Bi towards formate,[15,16] and Cu towards C-C coupled products like C_2H_4.[13,17] However, there are comparatively fewer reports on the functioning of these catalysts when integrated with CO_2R photocathodes. Hinogami et al.[18] interfaced p-Si with Cu, Ag, and Au without any ETL and found faradaic efficiencies (FEs) of up to ca. 30% for formate and methane for Cu and up to 50% for CO for Ag. Qiu et al.[19] reported a p-InP/TiO_2/Cu photocathode which, intriguingly, produced methanol at ca. 5% FE. Gurudayal et al.[20] reported a Si photocathode with a TiO_2 ETL and Cu-Ag bimetallic catalyst which produced up to 80% selectivity for C_2+ products. However, in this case, the thick catalyst layer was optically opaque so that illumination from the back (dry) side was employed.

It thus remains an unmet challenge to make a selective CO_2R photocathode capable of front (electrolyte) side illumination. In our initial attempts to make such a device we used p-Si/TiO_2 interfaced with Cu and Ag. However, under operation, the TiO_2 was reduced to Ti metal, which then dominates the catalytic activity and produces H_2 (FE > 97%).

We then examined the Si PV literature to find an oxide ETL which would be more stable than TiO_2; TaO_x appeared promising. When interfaced to Si, it has a small conduction band offset (desirable for electron collection) and large valence band offset (desirable for hole blocking) and

is reported to passivate surface states.[21–23] Si PV cells incorporating an n-Si/TaO_x heterocontact have been reported to have up to 19% power conversion efficiency.[21] TaO_x has also been used as an ETL for photocathodes. Wang et al[24] reported that a pn^+-Si/Ta_2O_5/Pt photocathode was stable for over 200 hours while generating H_2. Riyajuddin et al[25] reported 10 hours of stability under HER conditions for a Si nanowire/Ta_2O_5/N-doped graphene quantum dot photocathode.

The prior PV and PEC HER work with TaO_x suggests that it may be a good candidate for an ETL for PEC CO_2R devices. Moreover, examination of its Pourbaix diagram under typical CO_2R conditions (-1 V vs. SHE and pH 7) predicts that it will be stable.[26,27] There is also considerable synthesis flexibility. TaO_x thin films have been prepared by a variety of techniques like pulsed laser deposition (PLD)[28], RF sputtering[29] and atomic layer deposition (ALD)[30] and its electronic conductivity can be tuned (from insulating to semiconducting) by controlling the concentration of oxygen vacancies.[31]

These considerations motivated us to study p-Si/TaO_x photocathodes interfaced with thin (optically transparent) metal CO_2R catalysts. We synthesized TaO_x thin films using pulsed laser deposition (PLD) and reactive radio frequency (RF) sputtering techniques. Stoichiometric Ta_2O_5 films had poor electronic transport which was improved by controlling the oxygen partial pressure during deposition. Under simulated AM 1.5G illumination, the TaO_x ETL-based Si photocathodes (synthesized by both PLD and RF sputtering) had good selectivity to CO_2R products, ~50% and ~30% respectively, which we attribute to the stability and inertness of the TaO_x. Using ion implanted contacts onto silicon photocathodes with TaO_x ETLs higher photovoltages were obtained (n^+ on p-Si ~ 430 mV and p^+ and n^+ on n-Si ~ 460 mV) when compared to p-Si/TaO_x junction (~ 300 mV). We found that the photocathodes were quite sensitive to contamination from metal crossover from the anode due to the small catalyst loading needed for optical transparency and that this could be mitigated by using a non-noble metal counter electrode (graphite). We

identify stability as a key challenge for this type of solar to chemical energy conversion approach and provide scale-up scenarios informed by a technoeconomic analysis.

RESULTS AND DISCUSSION

TiO_2 as an ETL for CO_2R Si photocathodes with a thin Cu catalyst. In initial work, we investigated the CO_2R product distribution of a p-Si photocathode with an atomic layer deposition (ALD) TiO_2 as an ETL and a thin 10 nm Cu co-catalyst. PEC measurements were performed in 0.1 M $KHCO_3$ electrolyte under 1 sun illumination for Si photocathodes (these conditions were used throughout the study, see Detailed Methods section in the SI). Such a photocathode shows a photocurrent onset at ~ -0.05 V vs RHE and a photocurrent density of ~ 12 mA cm^{-2} at -1 V vs RHE (**Figure 1a).** However, the expected products from CO_2R on Cu are not observed. Instead, the major product is H_2 (FE >97%, **Figure 1b**).

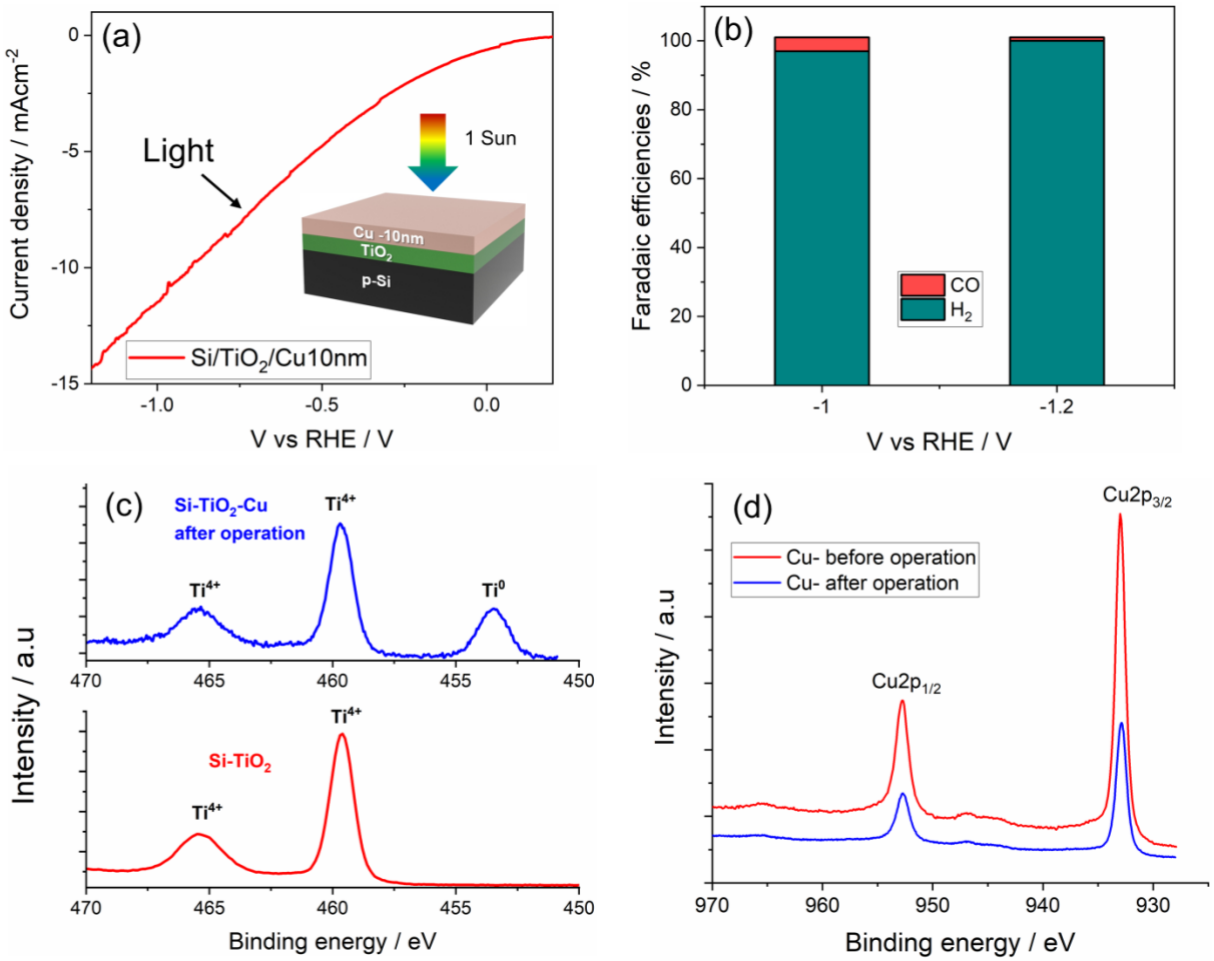

Figure 1. (a) Current density (*J*) vs Voltage (*V*) plots for Si/TiO_2/Cu10 nm under 1 sun illumination in 0.1 M $KHCO_3$ (b) Faradaic efficiencies of CO_2R products for pSi/TiO_2/Cu10 nm (c) Ti 2p core level spectra of Si-TiO_2 (as prepared from ALD) and Si-TiO_2-Cu10nm after CO_2R photo electrolysis for 230 mins under 1 sun illumination in 0.1M $KHCO_3$ at -1.0 V vs RHE (d) Cu 2p core level spectra of Si-TiO_2-Cu10nm before and after operation under 1 sun illumination in 0.1 M $KHCO_3$ at -1.0 V vs RHE.

We hypothesized that the H_2 formation was due to the activity of Ti metal, which is known to be active for HER.[13] Indeed, we see experimental evidence that when TiO_2 is in contact with the electrolyte (0.1 M $KHCO_3$) under CO_2R conditions, it is reduced to Ti metal as evidenced by the prominent Ti^0 peak in the Ti 2p core level spectra after operation (**Figure 1c**). Evidently, the HER

activity on the Ti outcompetes CO_2R on the Cu, which remain unmodified after operation (**Figure 1d**).

We investigated the effect of increasing the thickness of the Cu layer, understanding that this will eventually limit the photocurrent density in the front illumination geometry which we employed. Upon increasing the Cu thickness to 15 nm (**Figure S1**), we observed a marginal improvement with CO_2R FEs of ca. 10%. Further increases in the metal thickness would be expected to greatly reduce the photocurrent (**Figure S4**). We concluded that TiO_2 is not a suitable ETL for CO_2R photocathodes operated under the conditions we have employed and thus explored TaO_x as an alternative.

Pulsed Laser Deposition (PLD) grown TaO_x as an ETL for p-Si CO_2R photocathodes: Next, we synthesized TaO_x films on p-Si by PLD using a stoichiometric Ta_2O_5 target (details in SI). Substoichiometric Ta_2O_5 has been reported to exhibit higher electronic conductivity than more stoichiometric material due to the presence of oxygen vacancies.[32] Therefore, different O_2 flow rates were employed in the PLD chamber as shown schematically in **Figure 2 (a)**. We denote TaO_x grown by PLD on p-Si with 0.1 sccm, 0.3 sccm and 1.6 sccm oxygen flow as TaO_x-0.1, TaO_x-0.3 and TaO_x-1.6. As expected from prior reports on PLD-grown TaO_x without any annealing step,[33] XRD patterns (**Figure S2)** were featureless, indicating that the films are amorphous.

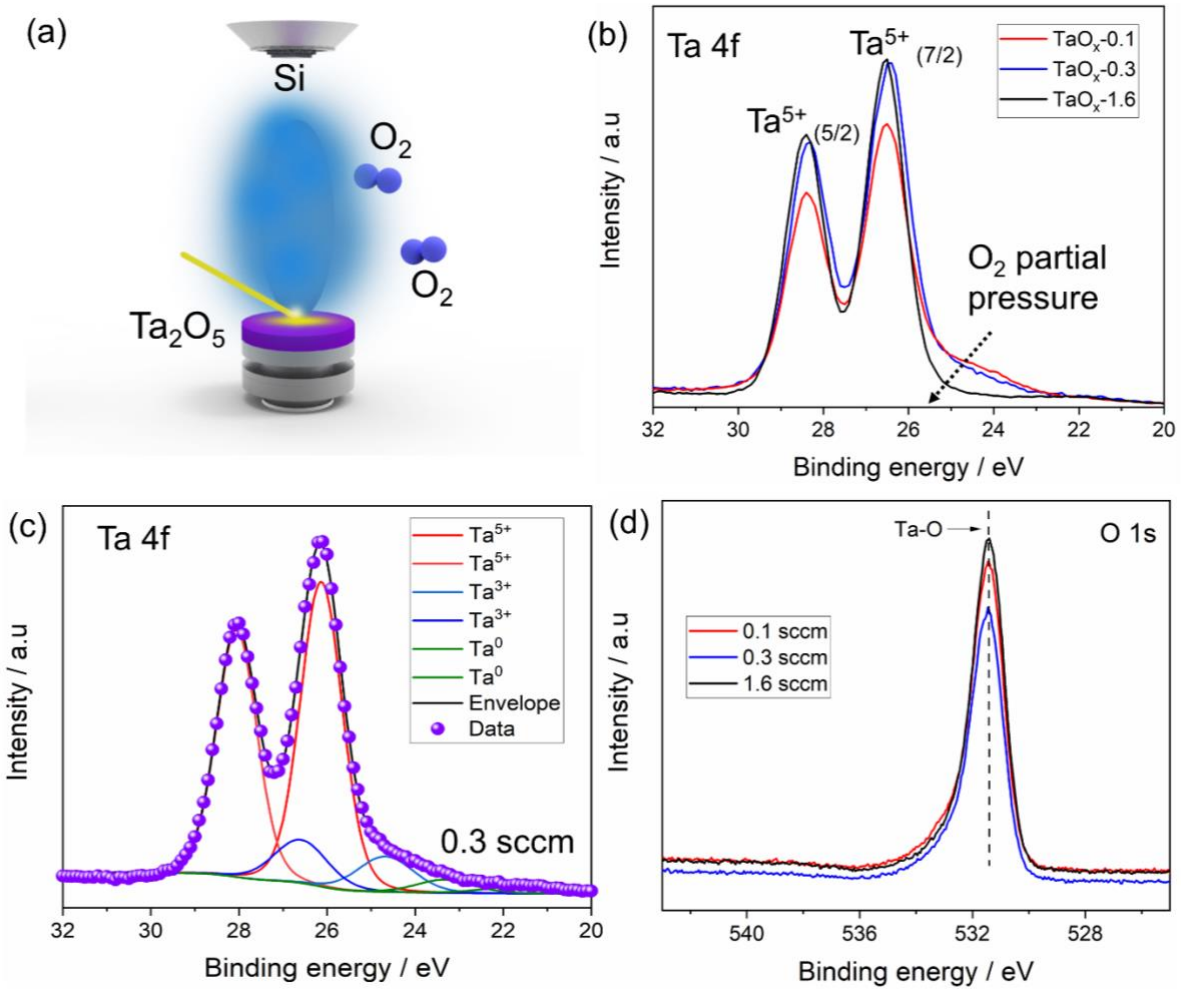

Figure 2. (a) Schematic of PLD deposition of TaO_x (b) XPS core level spectra of Ta 4f for PLD-grown TaO_x grown at different oxygen flow rates (c) XPS core level spectra of Ta 4f for TaO_x-0.3(d) XPS core level spectra of O1s for PLD-grown TaO_x at different oxygen flow rates.

Chemical composition was evaluated with X-ray photoelectron spectroscopy (XPS). We assign the doublet peak observed at 28.3/26.4 eV for all films (**Figure 2 (b)**) to Ta 4f 7/2 and Ta 4f 5/2 from the Ta^{5+} oxidation state.[34] A notable feature of the Ta 4f spectra is the presence of a shoulder peak at between 25 eV and 23 eV which decreases with increasing O_2 flow rate in the PLD chamber. We assign this feature to sub-oxides of Ta which are expected to be formed in substoichiometric Ta_2O_5 films.[35]

Higher flow rates of O_2 (1.6 sccm) yielded a more stoichiometric Ta_2O_5 film as evidenced by the absence of suboxides of tantalum oxide. **Figure 2 ©** shows the deconvolution of the Ta 4f spectra of TaO_x-0.3. Focusing on the shoulder at lower binding energy, the peaks at 26.4 eV and 24.5 eV are attributed to the Ta^{3+} oxidation state.[29,36] The O 1s spectrum was fitted with two gaussian components with peaks at 530.9 eV and 532 eV which would correspond to Ta-O binding and surface contaminations/ peroxide O_2^{2-} (**Figure S3**).[21,34] No obvious difference was observed for the O 1s spectra for the different O_2 flow rates of the TaO_x films (**Figure 2 (d)**) with the peak position of the Ta-O binding remaining the same for all thin films. Our XPS results shows that the stoichiometry of TaO_x could be controlled by varying the O_2 flow rate in the PLD chamber.

Next, we fabricated p-Si photocathodes with the PLD-grown TaO_x as the ETL and Cu co-catalyst. We chose a Cu catalyst thickness of 10 nm due to higher CO_2R product yield and higher photocurrent density (despite having lower transmission of light to the photocathode than a 5 nm thick Cu co-catalyst) (**Figure S4-S6**). Si photocathodes with a TaO_x-0.3 ETL exhibited the highest photocurrent density under CO_2R conditions reaching a maximum photocurrent density of ~ 7 mA cm^{-2} (**Figure 3 (a)**). The photocurrent density of TaO_x-1.6 was lower than the TaO_x-0.3 due to its higher resistivity as result of a higher oxygen partial pressure during the PLD growth.[31,36]. This was verified by performing ultraviolet photoelectron spectroscopy (UPS) measurements to obtain the valence band spectra of TaO_x (**Figure 3 (b)**). It is evident that the defect band in the band gap of TaO_x increases with reduced oxygen partial pressure confirming the increase of oxygen vacancies for PLD TaO_x grown with a 0.3 sccm O_2 flow rate. The p-Si/TaO_x/Cu-10nm based photocathode produced nearly 52 % CO_2R products at bias of -1.2 V vs RHE while a p-Si/TiO_2 photocathode with the same Cu co-catalyst thickness yielded only H_2 (**Figure 4 (a))** despite its earlier photocurrent onset and higher photocurrent density (**Figure S7**).

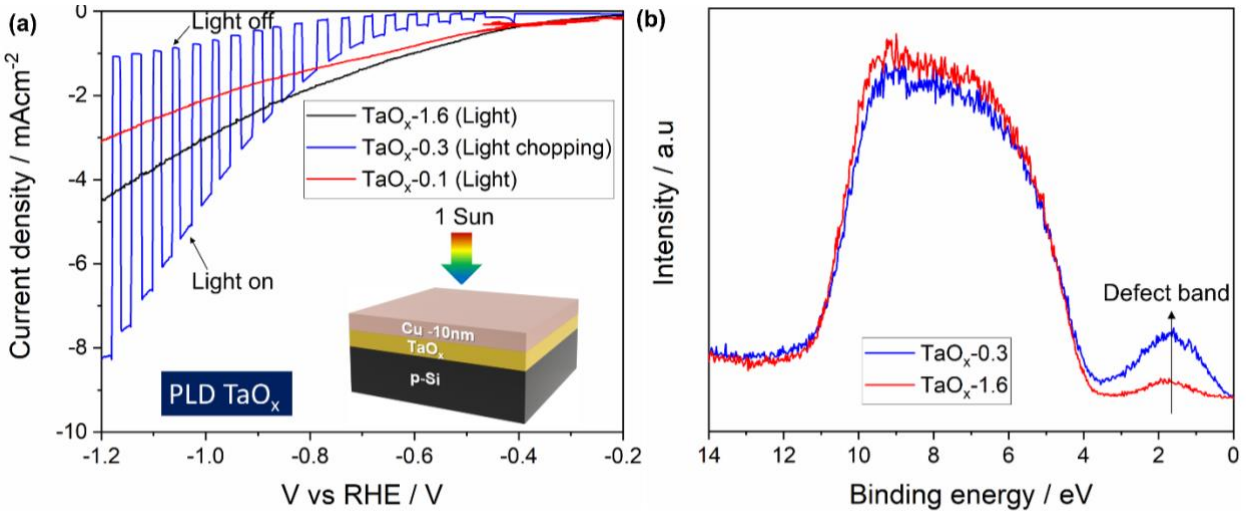

Figure 3. (a) Current density vs Voltage plots for p-Si/TaO_x/Cu 10nm photocathodes with TaO_x grown ETLs at different oxygen flow rates under 1 sun illumination in a 0.1 M $KHCO_3$ electrolyte. (b) Valence band spectra of TaO_x-0.3 and TaO_x-1.6 thin films.

To evaluate the compatibility of TaO_x with other CO_2R catalysts, an Au catalyst was employed to evaluate the CO_2R product distribution. A Ta underlayer was used for the Au catalyst to improve its adhesion to TaO_x. The photocurrent density obtained was similar to that of p-Si/TaO_x/Cu (**Figure S8**) and the CO_2R products obtained were primarily C1products (CO, $HCOO^-$) as expected for an Au catalyst (**Figure 4 (b)**). Based on these results, TaO_x could be employed as an ETL for p-Si interfaced with both Cu and Au co-catalysts for CO_2R.

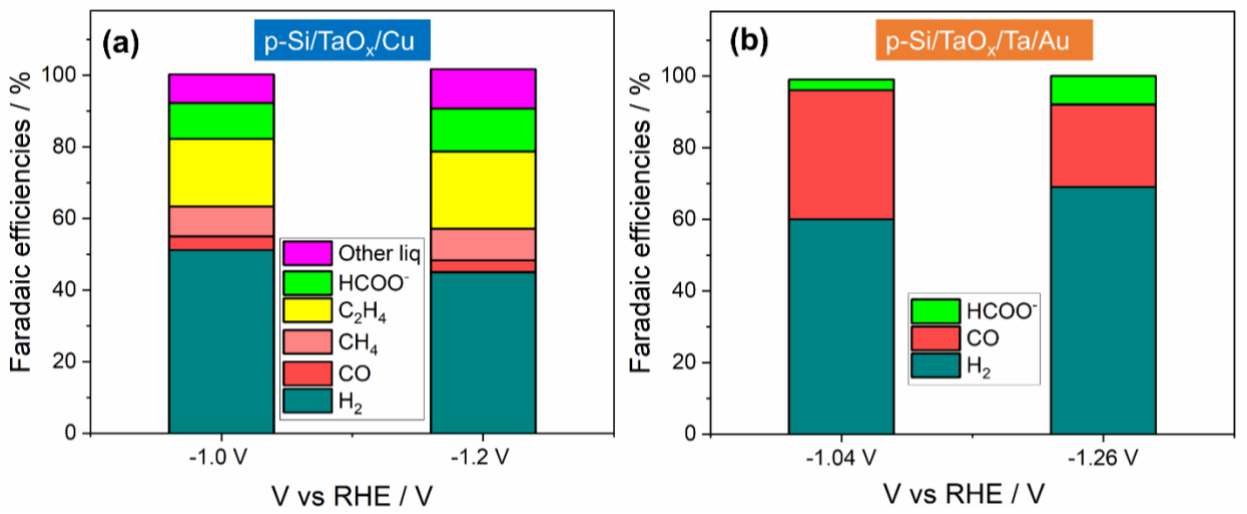

Figure 4. Faradaic efficiencies for (a) p-Si/TaO_x/Cu (other liq - ethanol, propanol) (b) p-Si/TaO_x/Ta/Au photocathodes under 1 sun illumination in 0.1 M $KHCO_3$

Reactive radio frequency (RF) sputtered TaO_x as an ETL for CO_2R Si photocathode. Photocathodes were made with TaO_x deposited by reactive RF sputtering, which is a more scalable technique than PLD (**experimental details in supporting information**). A Ta metal target was used and the Ar:O_2 ratio in the chamber was used to oxygen substoichiometry of TaO_x. **Figure 5 (a)** shows the Ta 4f spectra for the TaO_x films prepared with 2 different Ar:O_2 ratios. Similar to the PLD prepared TaO_x films (compare **Figure 2 (b)**), the doublet peaks for Ta^{5+} oxidation state are dominant. However, the film made with a lower O_2 partial pressure (99:1 Ar:O_2) exhibits a significant peak corresponding to Ta metal suggesting that not all the Ta metal has been oxidized to the +5 oxidation state.

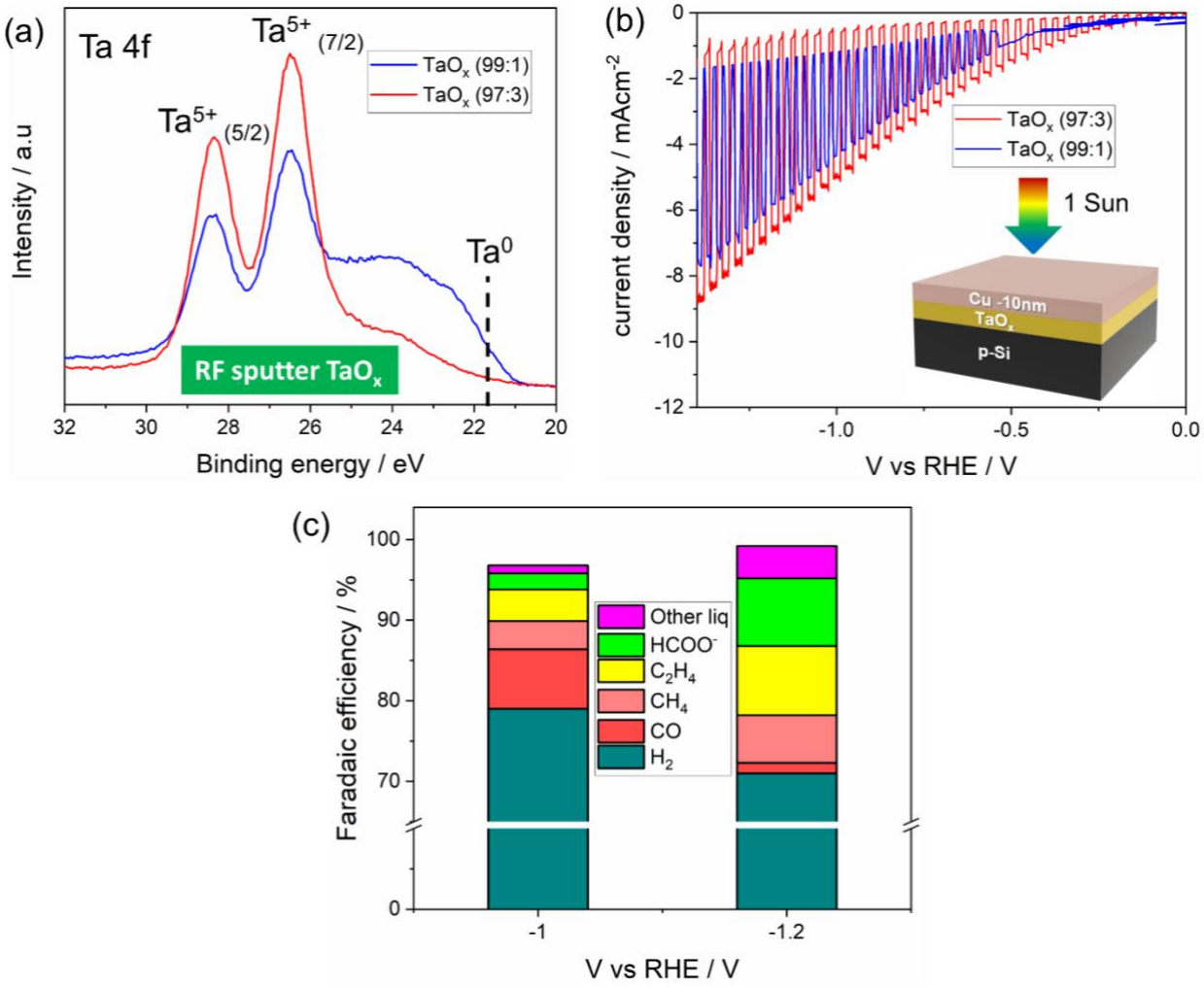

Figure 5. (a) Ta 4f core level spectra of TaO_x prepared by RF sputtering under 2 different Ar: O_2 ratio (b) Current density (*J*) vs Voltage (*V*) plots for Si/TaO_x(20 nm)/Cu 10 nm under 1 sun illumination in 0.1 M $KHCO_3$ under 2 different Ar:O_2 concentration (c) Faradaic efficiencies of CO_2R products for Si/TaO_x (20 nm)/Cu10 nm under -1 V and -1.2 V vs RHE.

Photocathodes were fabricated using the same device architecture and CO_2R conditions as the PLD deposited TaO_x and the photocathode with higher oxygen content (TaO_x 97:3) yielded a marginal higher photocurrent and lower dark current as there is no Ta metal in the film when compared to TaO_x (99:1) (**Figure 5 (b)**). Variation of the TaO_x thickness showed that photocathodes with 20 nm TaO_x yielded better fill factors and photocurrent density despite exhibiting similar substoichiometry **(Figure S9 and S10**). If the TaO_x thickness is too thick as in

the case of 40nm then the photocurrent density is lowered probably due to increased series resistance and if the thickness is below 20 nm then the coverage of TaO_x on Si is not uniform. Hence a thickness of 20 nm of TaO_x with 97:3 Ar to O_2 condition was found to be optimum. Upon comparing the champion device of sputtering (TaO_x (97:3)) with PLD champion device (TaO_x-0.3), the sputtering champion device exhibited an earlier photocurrent onset but a marginally lower photocurrent density (**Figure S11**). This could be attributed to an increase in the substoichiometry of TaO_x films prepared by sputtering (**Figure S12**).

Si photocathode with dual ETL: A dual ETL approach has shown promise in water splitting where one ETL serves as a n-type junction layer and the other performs the role of protection and catalyst support.[37] Since TiO_2 has a better band alignment with p-Si, we used it as the primary ETL and sputtered TaO_x on it to take advantage of its higher CO_2R product yield and stability. The photocurrent onset and the photocurrent density of such a dual ETL photocathode is lower in comparison to Si-TiO_2/Cu TiO_2/TaO_x layer **(Figure 6 (a))**. But the dual ETL photocathode produced more CO_2R products than a Si-TiO_2-Cu as the TiO_2 is buried under TaO_x. Since the TiO_2 layer is not fully exposed to the electrolyte under CO_2R conditions, HER activity is suppressed and the catalytic activity could be dominated by the TaO_x/Cu layer **(Figure 6b)**. Having a dual ETL approach would enable photocathode designs where the photovoltage could be improved by employing n-type layer which has a good band alignment with the underlying p-type absorber and simultaneously taking advantage of TaO_x/Cu's stability and higher yield of CO_2R products.

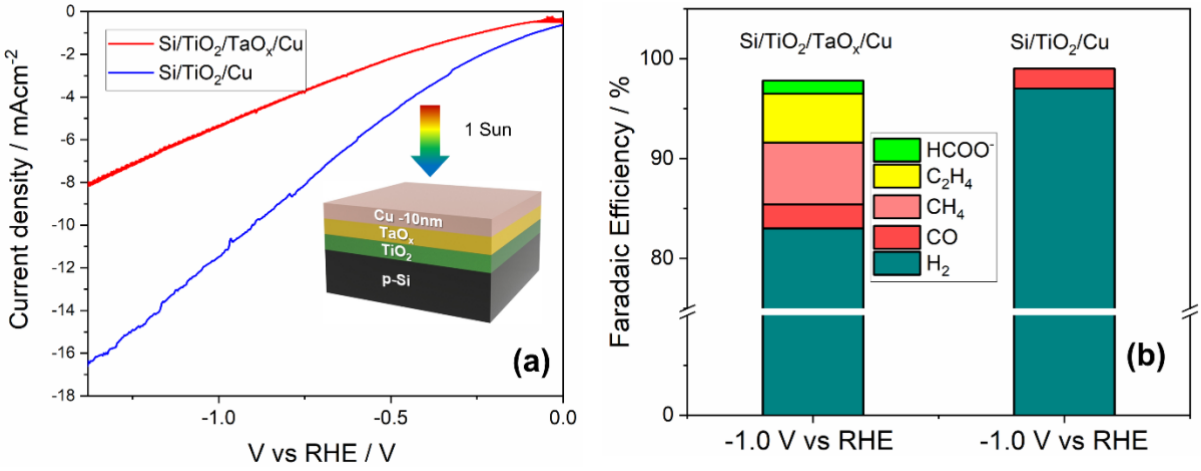

Figure 6. (a) Current density (*J*) vs Voltage (*V*) plots for Si/TiO_2/Cu and Si/TiO_2/TaO_x (97:3)/Cu under 1 sun illumination in 0.1 M $KHCO_3$ (b) Faradaic efficiencies of CO_2R products for Si/TiO_2/Cu and Si/TiO_2/TaO_x(97:3)/Cu The thickness of Cu catalyst used was 10 nm for both photocathodes.

Photovoltage: Finally, we fabricated a n^+Si/TaO_x (97:3)/Cu dark cathode (black curve in Figure 7) so that we can compare the onset of the dark catalytic current to photocurrent onset of a p-Si/TaO_x/Cu photocathode (Figure 7 (a)). There are no reports in literature to the best of our knowledge where p-Si is directly interfaced with TaO_x to form the p-n junction which gives a photovoltage. Instead, most reports in the photovoltaic literature employ n-Si with TaO_x as a surface passivation/electron selective contact.[21] In this work a photovoltage of ~ 300 mV was obtained for p-Si/TaO_x junctions with a Cu CO_2R catalyst (**Figure 7 (a) and Figure S13 (a)**). To improve the photovoltage of these photocathodes, an n^+ implant of p-Si wafers was performed to yield a better-quality junction with RF sputtered TaO_x onto the p-Si/n^+ with a Cu catalyst. This photocathode yielded a higher photovoltage of 430 mV (**Figure 7 (b) and Figure S13 (b)**). Both photovoltage and photocurrent density was increased when a silicon photocathode (n-Si with n^+ and p^+ implanted contacts[20]) were employed with a RF-sputtered TaO_x ETL and Cu catalyst

(**Figure 7 (c) and Figure S13 (c)**) showing the broad applicability of RF-sputtered TaO_x as an ETL for photocathodes.

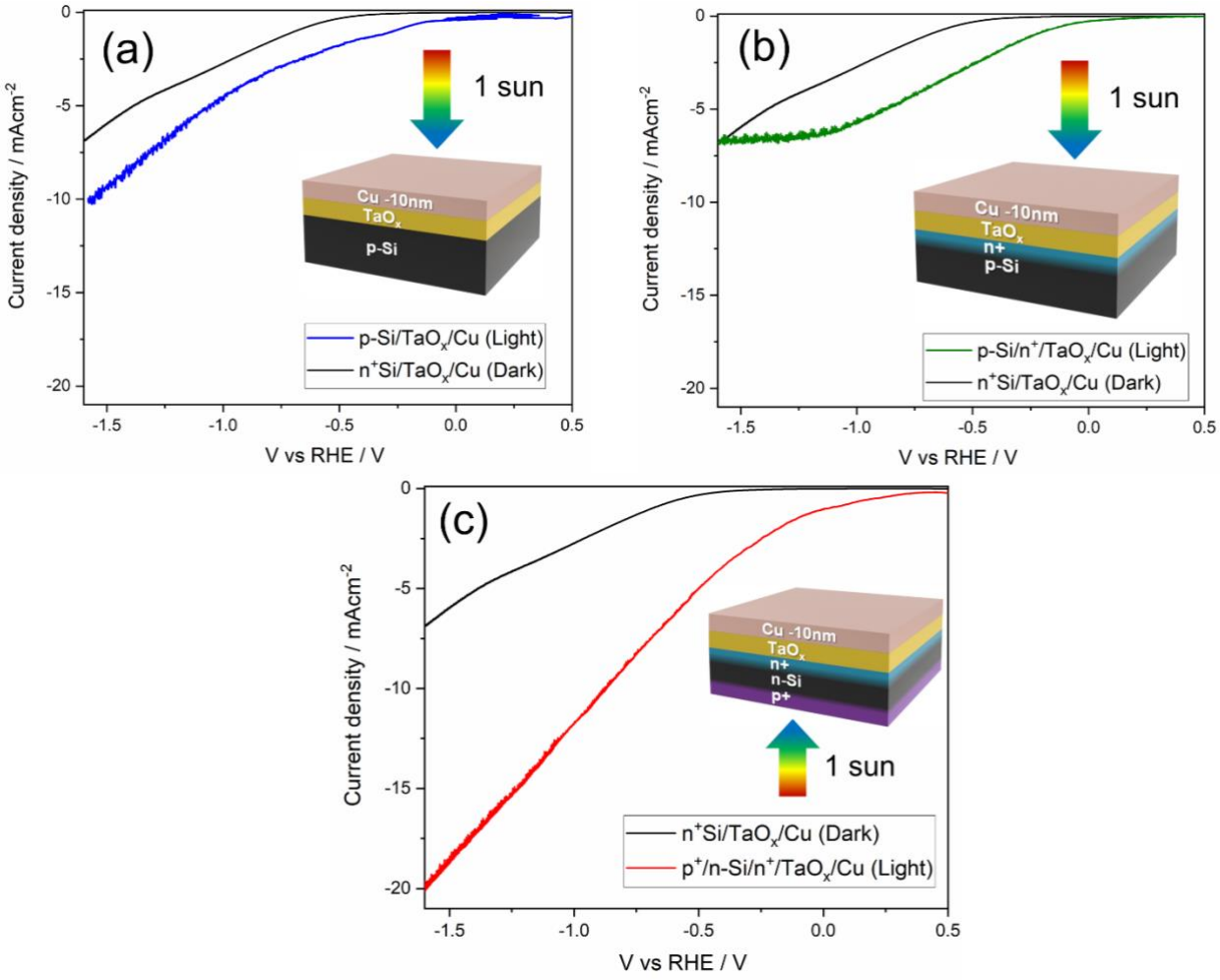

Figure 7. Current density vs voltage plots for (a) $n^+Si/TaO_x/Cu$ (dark cathode) and $p\text{-}Si/TaO_x/Cu$ (photocurrent), (b) $n^+Si/TaO_x/Cu$ (dark cathode) and $p\text{-}Si/n^+/TaO_x/Cu$ (photocathode) and (c) $n^+Si/TaO_x/Cu$ (dark cathode) and $p^+/n\text{-}Si/n^+/TaO_x/Cu$ (photocathode).

Long-term stability of p-Si/TaO_x/Cu photocathodes: The long-term stability of $p\text{-}Si/TaO_x/Cu$ photocathodes over a period of 300 mins was evaluated by the time evolution of CO_2R gaseous products (**Figure S14**). A fairly stable evolution of CO_2R products was observed for at least for a

period of 120 mins after which the faradaic efficiencies for the CO_2R products decreased. The electrolyte was changed after 225 mins when no ethylene production was observed. Although there was a decrease in the Cu signal from XPS after operation (**Figure S15**), the lack of ethylene production could not be just attributed to loss of Cu catalyst. After CO_2R photoelectrolysis, contact angle measurements were performed to investigate the hydrophobicity of the photocathode and it was observed that the surface of the photocathode (TaO_x/Cu) became more hydrophilic after CO_2R (**Figure S16)**). In the CO_2R electrolysis literature, the change in hydrophobicity has been attributed to minor CO_2R product polymerization (acrolein to polyacrylic acid) on the surface of the Cu catalyst.[38] It is conceivable that this effect is occurring here, as well. In stability tests, we used a Pt counter electrode but found that Pt migration to the PEC surface strongly affected the results which are mitigated by using a graphite counter electrode (see discussion in SI).

Using a graphite counter electrode resulted in continued ethylene production even after 300 mins of operations when compared to Pt counter electrode which required change of electrolyte after 225 mins in order to sustain ethylene production (**Figure 8 (a)**). Further no Pt 4f peak (71 eV) was observed on the photocathode surface after 5 hours of operation when employing a graphite counter electrode (**Figure S17**). The surface of p-Si/TaOx/Cu after operation were still hydrophilic hinting that the long-term stability of the photocathode was not significantly affected by the change in hydrophobicity of the surface but rather the crossover of Pt from the counter electrode (**Figure 8 (b) and (c)**).

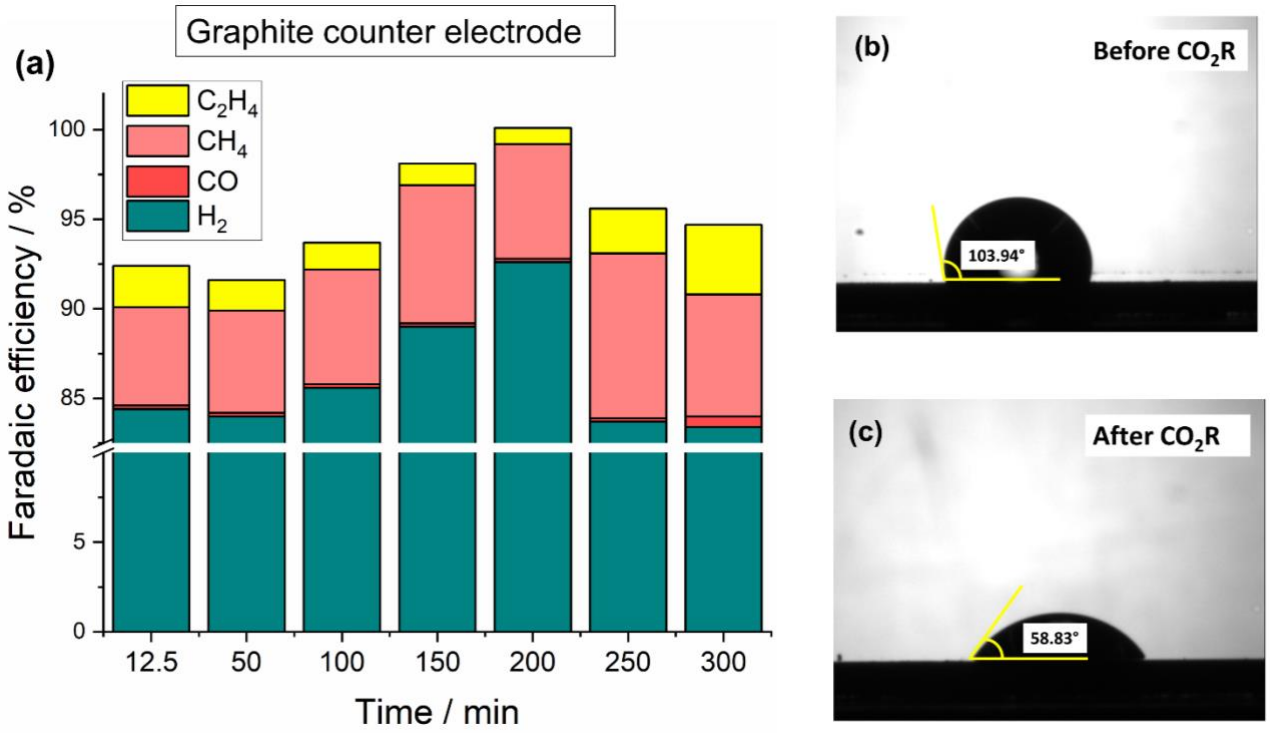

Figure 8. (a) Gaseous CO_2R product distribution as a function of time for Si/TaO_x(97:3)/Cu10nm photocathode under 1 sun illumination in 0.1M $KHCO_3$ at -1.2 V vs RHE with a graphite counter electrode where the production of C_2H_4 remained steady after 300 mins of operation without any need of electrolyte change. Contact angle measurements of p-Si/TaO_x/Cu photocathode with a Pt counter electrode during CO_2R measurements for (b) before CO_2R and (c) after CO_2R operation for 300 mins.

Techno-economic analysis of Si-TaO_x-Cu photocathode: The selectivity of Si-TaO_x-Cu photocathode towards carbon-containing products incentivized to conceptually design a large-scale photocatalytic system that could be used for production of carbon-rich gas streams from abundant, biogenic CO_2 (**Figure. 9(a)**). One of the anticipated bottlenecks towards the deployment of CO_2-based systems is the low concentration of CO_2 in the ambient air.[39] The availability of CO_2 in oceans is significantly higher.[40] We thus conceptualized a system where ocean water, source of preconcentrated CO_2, circulates through photoelectrochemical systems, and CO_2 is converted into

a stream of ethylene, carbon monoxide, methane, and hydrogen, being a useful input to various chemical manufacturing processes.[41] Such a system would require a minimum input of renewable electricity sourced from solar panels or windmills, as a significant amount of energy is being supplied via direct sunlight irradiation.

Looking towards this large-scale scenario, we sought to understand whether proposed catalyst deposition method could be effectively scaled up, and we assessed the cost of production of a system incorporating a thin TaO_x-Cu layer deposited on silicon wafer, using pilot plant scale/ semi-industrial coefficients for energy and gases use during physical vapor deposition process[42,43], and most recent price indicators for each component of the electrocatalytic system.[44–47] While other deposition methods reported here, such as RF sputtering, could further reduce the catalyst production cost, selecting physical vapor deposition (PVD) as reference allows to assess a less favorable scenario thus reduce the risk of overestimating the potential of the photocathode, being current at an early development stage. Given the excellent reduction of the thickness of the catalyst, the manufacturing cost becomes practically reduced to the cost of the silicon wafer and the membrane (**Figure 9(b)**), contributing together to >95% of the cost of the photoelectrode system (detail cost contributions in SI). Intriguingly, similar results have been obtained for Au-based electrodes (SI), showing that thin catalyst layers allow to drastically minimize the cost of metals used in catalyst development.

Looking at the return on investment into the proposed photoelectrochemical system, we deployed a recent protocol for the assessment of emerging electrolysis technologies (method details in SI) [48]. Our assessment is based on a model of a Si-TaO_x-Cu electrolyzer where 75% of supplied CO_2 is being converted to a carbon-rich product, under experimentally reported 0.01 A cm^{-2} of current density and applying an external voltage of 1.2 V. We assumed an average market price for this ethylene-rich stream, current renewable electricity price[41] between 0.02 – 0.05 $/kWh, and a

broad range of CO_2 credit being paid for the avoided emissions of CO_2 (our system allows to avoid emissions of petroleum-based CO_2 by producing chemicals from biogenic CO_2). The sensitivity analysis **(Figure 9(c))** demonstrates that in presence of CO_2 credit schemes, return on investment is even less than 2 years, what provides an incentive for further research and optimization of CO_2 utilization methods. The decrease of the price of renewable electricity alone would not be sufficient to support these innovative approaches (see the grey area in **Figure 9 (c)**), depicting non-viable scenarios), and the availability of CO_2 credit will be critical for the growth of photoelectrochemical methods. Still, we need as well to address several scale-up challenges: demonstrate the capability to achieve increased CO_2 conversion level and avoid the formation of liquid products which will be more difficult to separate than the gaseous stream that we focus on.

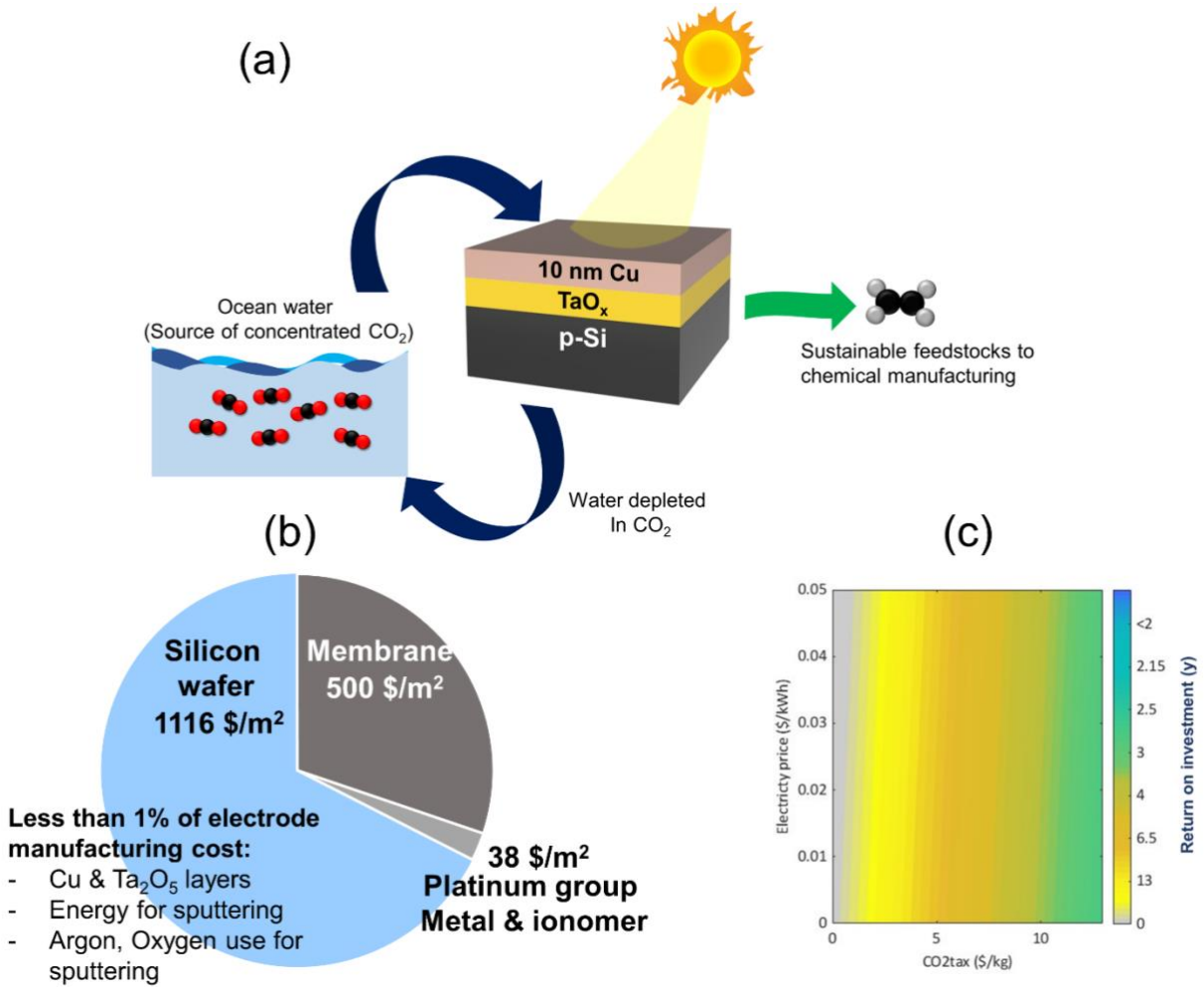

Figure 9. Conceptualized scale-up and techno-economic analysis (TEA) of systems incorporating Si/TaO_x/Cu photocathodes: (a) concept of biogenic CO_2- based manufacturing systems, (b) manufacturing cost for Si/TaO_x/Cu photocathodes based on pilot-plant/semi industrial scale coefficient for energy and gases uses during PVD process, (c) sensitivity analysis for the return on investment for the entire photoelectrochemical system, as a function of renewable electricity price and imposed credit for avoided CO_2 emissions. Grey area depicts scenarios which are not economically viable. Methodology details are given in the SI.

CONCLUSION

In summary, TaO_x was used as an ETL for Si photocathodes (Si/TaO_x p-n junction) for the first time for CO_2R. We first identified the major drawback of employing TiO_2 as an ETL (reduction of TiO_2 to Ti metal and evolution of H_2) and then synthesized TaO_x by 2 different synthesis techniques (PLD and RF sputtering). The electron selectivity of the TaO_x ETLs was tuned by controlling the oxygen partial pressures during thin film deposition for both techniques. Si/TaO_x/Cu photocathodes yielded much higher CO_2R products (52% for PLD TaO_x and 30% for RF sputtered TaO_x)) when compared with Si/TiO_2/Cu photocathode. We also demonstrated a dual ETL layer (Si/TiO_2/TaO_x/Cu) photocathode which could be a possible strategy for other photocathodes to suppress HER and yield more CO_2R products. The photovoltage of silicon photocathodes with TaO_x ETL/Cu catalyst was improved by using implanted contacts (n^+ only on p-Si & n^+ and p^+ contacts on n-Si) from 300 mV to 430-460 mV. For long term stability of these photocathodes, the limiting factor was the Pt crossover from the counter electrode to the Si/TaO_x/Cu photocathode. The photocathode was found to be stable (sustained ethylene production) for ~ 300 mins of CO_2R photoelectrolysis when employing a graphite counter electrode to mitigate Pt crossover. By employing scalable synthesis techniques (RF sputtering for ETLs and Cu catalyst) and simple device architecture without any energy intensive fabrication process (high temperature growth/doping of Si) we have demonstrated an excellent scalability of the system. Our techno-economic analysis outlines pathways to making the photoelectrochemical platform a viable method for decarbonized chemical production, and we determined the scale of CO_2 credits mechanisms necessary to support the growth of photocatalytic field. This work also elucidates possible design strategies of other ETLs for CO_2R photocathode- suppression of HER catalysis, good electronic conductivity and Pourbaix stability.

Author Contributions

The manuscript was written through contributions of all authors. All authors have given approval to the final version of the manuscript. RL, RRP, and JWA conceived the experiment. RRP, RL and MK performed the synthesis of TaO_x. RRP did the XPS measurements and RL performed the UPS measurements. Photocathodes were fabricated by RRP and RL. Liquid and Gas CO_2R product quantification was performed by RRP and RL. SS helped with long-term testing of photocathodes and graphics in the paper. IDT performed the XRD measurements. END performed the MEEP simulations. MB performed the technoeconomic analysis (TEA) and wrote the TEA part. RRP and JWA wrote the original draft of the paper. All authors were involved in the reviewing and editing of the draft. JWA was involved in the funding acquisition and project administration.

Conflict of interest

The authors declare no competing financial interests.

ACKNOWLEDGMENT

This material is based on work performed by the Liquid Sunlight Alliance, which is supported by the U.S. Department of Energy, Office of Science, Office of Basic Energy Sciences, Fuels from Sunlight Hub under Award Number DE-SC0021266. Technoeconomic analyses performed by MB were supported by the National Research Foundation (NRF), Prime Minister's Office, Singapore, under its Campus for Research Excellence and Technological Enterprise (CREATE) programme through the eCO2EP project NRF2016-ITC001-005 operated by the Cambridge Centre for Advanced Research and Education in Singapore (CARES) and the Berkeley Educational Alliance for Research in Singapore (BEARS). RRP acknowledges fellowship support from the Swiss National Science Foundation Early Postdoc Mobility Program (191299). MK acknowledges fellowship support from the Brain Korea 21 Program (BK21 FOUR). END acknowledges

fellowship support from EPFL and the Heyning-Roelli Schindler Foundation. IDT acknowledges fellowship support from the Erasmus Foundation.

REFERENCES

(1) Wurfel, U.; Cuevas, A.; Wurfel, P. Charge Carrier Separation in Solar Cells. *IEEE J. Photovoltaics* **2015**, *5* (1), 461–469. https://doi.org/10.1109/JPHOTOV.2014.2363550.

(2) Taguchi, M.; Yano, A.; Tohoda, S.; Matsuyama, K.; Nakamura, Y.; Nishiwaki, T.; Fujita, K.; Maruyama, E. 24.7% Record Efficiency HIT Solar Cell on Thin Silicon Wafer. *IEEE J. Photovoltaics* **2014**, *4* (1), 96–99. https://doi.org/10.1109/JPHOTOV.2013.2282737.

(3) Battaglia, C.; Cuevas, A.; De Wolf, S. High-Efficiency Crystalline Silicon Solar Cells: Status and Perspectives. *Energy Environ. Sci.* **2016**, *9* (5), 1552–1576. https://doi.org/10.1039/C5EE03380B.

(4) Chavali, R. V. K.; De Wolf, S.; Alam, M. A. Device Physics Underlying Silicon Heterojunction and Passivating-Contact Solar Cells: A Topical Review. *Progress in Photovoltaics: Research and Applications*. 2018. https://doi.org/10.1002/pip.2959.

(5) Allen, T. G.; Bullock, J.; Yang, X.; Javey, A.; De Wolf, S. Passivating Contacts for Crystalline Silicon Solar Cells. *Nat. Energy* **2019**, *4* (11), 914–928. https://doi.org/10.1038/s41560-019-0463-6.

(6) Campet, G.; Puprichitkun, C.; Sun, Z. W. Protection of Photoanodes against Photocorrosion by Surface Deposition of Oxide Films: Criteria for Choosing the Protective Coating. *J. Electroanal. Chem. Interfacial Electrochem.* **1989**, *269* (2), 435–445. https://doi.org/10.1016/0022-0728(89)85150-2.

(7) Hu, S.; Lewis, N. S.; Ager, J. W.; Yang, J.; McKone, J. R.; Strandwitz, N. C. Thin-Film Materials for the Protection of Semiconducting Photoelectrodes in Solar-Fuel Generators. *J. Phys. Chem. C* **2015**, *119* (43), 24201–24228. https://doi.org/10.1021/acs.jpcc.5b05976.

(8) Chen, S.; Wang, L.-W. Thermodynamic Oxidation and Reduction Potentials of Photocatalytic Semiconductors in Aqueous Solution. *Chem. Mater.* **2012**, *24* (18), 3659–3666. https://doi.org/10.1021/cm302533s.

(9) Lin, Y.; Battaglia, C.; Boccard, M.; Hettick, M.; Yu, Z.; Ballif, C.; Ager, J. W.; Javey, A. Amorphous Si Thin Film Based Photocathodes with High Photovoltage for Efficient Hydrogen Production. *Nano Lett.* **2013**, *13* (11), 5615–5618. https://doi.org/10.1021/nl403265k.

(10) Lin, Y.; Kapadia, R.; Yang, J.; Zheng, M.; Chen, K.; Hettick, M.; Yin, X.; Battaglia, C.; Sharp, I. D.; Ager, J. W.; Javey, A. Role of TiO 2 Surface Passivation on Improving the Performance of P-InP Photocathodes. *J. Phys. Chem. C* **2015**, *119* (5), 2308–2313. https://doi.org/10.1021/jp5107313.

(11) Bae, D.; Seger, B.; Hansen, O.; Vesborg, P. C. K.; Chorkendorff, I. Durability Testing of Photoelectrochemical Hydrogen Production under Day/Night Light Cycled Conditions. *ChemElectroChem* **2019**, *6* (1), 106–109. https://doi.org/10.1002/celc.201800918.

(12) Hori, Y.; Murata, A.; Takahashi, R. Formation of Hydrocarbons in the Electrochemical Reduction of Carbon Dioxide at a Copper Electrode in Aqueous Solution. *J. Chem. Soc.*

Faraday Trans. 1 Phys. Chem. Condens. Phases **1989**, *85* (8), 2309. https://doi.org/10.1039/f19898502309.

(13) Hori, Y. Electrochemical CO_2 Reduction on Metal Electrodes. In *Modern Aspects of Electrochemistry*; Springer New York: New York, NY, 2008; Vol. 29, pp 89–189. https://doi.org/10.1007/978-0-387-49489-0_3.

(14) Chen, Y.; Li, C. W.; Kanan, M. W. Aqueous CO 2 Reduction at Very Low Overpotential on Oxide-Derived Au Nanoparticles. *J. Am. Chem. Soc.* **2012**, *134* (49), 19969–19972. https://doi.org/10.1021/ja309317u.

(15) Han, N.; Wang, Y.; Yang, H.; Deng, J.; Wu, J.; Li, Y.; Li, Y. Ultrathin Bismuth Nanosheets from in Situ Topotactic Transformation for Selective Electrocatalytic CO2 Reduction to Formate. *Nat. Commun.* **2018**, *9* (1), 1320. https://doi.org/10.1038/s41467-018-03712-z.

(16) Fan, L.; Xia, C.; Zhu, P.; Lu, Y.; Wang, H. Electrochemical CO2 Reduction to High-Concentration Pure Formic Acid Solutions in an All-Solid-State Reactor. *Nat. Commun.* **2020**, *11* (1), 3633. https://doi.org/10.1038/s41467-020-17403-1.

(17) Nitopi, S.; Bertheussen, E.; Scott, S. B.; Liu, X.; Engstfeld, A. K.; Horch, S.; Seger, B.; Stephens, I. E. L. L.; Chan, K.; Hahn, C.; Nørskov, J. K.; Jaramillo, T. F.; Chorkendorff, I. Progress and Perspectives of Electrochemical CO_2 Reduction on Copper in Aqueous Electrolyte. *Chem. Rev.* **2019**, *119* (12), 7610–7672. https://doi.org/10.1021/ACS.CHEMREV.8B00705.

(18) Hinogami, R.; Nakamura, Y.; Yae, S.; Nakato, Y. An Approach to Ideal Semiconductor Electrodes for Efficient Photoelectrochemical Reduction of Carbon Dioxide by Modification with Small Metal Particles. *J. Phys. Chem. B* **1998**, *102* (6), 974–980. https://doi.org/10.1021/jp972663h.

(19) Qiu, J.; Zeng, G.; Ha, M.-A.; Ge, M.; Lin, Y.; Hettick, M.; Hou, B.; Alexandrova, A. N.; Javey, A.; Cronin, S. B. Artificial Photosynthesis on TiO 2 -Passivated InP Nanopillars. *Nano Lett.* **2015**, *15* (9), 6177–6181. https://doi.org/10.1021/acs.nanolett.5b02511.

(20) Gurudayal; Beeman, J. W.; Bullock, J.; Wang, H.; Eichhorn, J.; Towle, C.; Javey, A.; Toma, F. M.; Mathews, N.; Ager, J. W. Si Photocathode with Ag-Supported Dendritic Cu Catalyst for CO2 Reduction. *Energy Environ. Sci.* **2019**, *12* (3), 1068–1077. https://doi.org/10.1039/c8ee03547d.

(21) Wan, Y.; Karuturi, S. K.; Samundsett, C.; Bullock, J.; Hettick, M.; Yan, D.; Peng, J.; Narangari, P. R.; Mokkapati, S.; Tan, H. H.; Jagadish, C.; Javey, A.; Cuevas, A. Tantalum Oxide Electron-Selective Heterocontacts for Silicon Photovoltaics and Photoelectrochemical Water Reduction. *ACS Energy Lett.* **2018**, *3* (1), 125–131. https://doi.org/10.1021/acsenergylett.7b01153.

(22) Wan, Y.; Bullock, J.; Cuevas, A. Passivation of C-Si Surfaces by ALD Tantalum Oxide Capped with PECVD Silicon Nitride. *Sol. Energy Mater. Sol. Cells* **2015**, *142*, 42–46. https://doi.org/https://doi.org/10.1016/j.solmat.2015.05.032.

(23) Greiner, M. T.; Helander, M. G.; Tang, W.-M.; Wang, Z.-B.; Qiu, J.; Lu, Z.-H. Universal Energy-Level Alignment of Molecules on Metal Oxides. *Nat. Mater.* **2012**, *11* (1), 76–81. https://doi.org/10.1038/nmat3159.

(24) Wang, T.; Liu, S.; Li, H.; Li, C.; Luo, Z.; Gong, J. Transparent Ta2O5 Protective Layer for Stable Silicon Photocathode under Full Solar Spectrum. *Ind. Eng. Chem. Res.* **2019**, *58* (14), 5510–5515. https://doi.org/10.1021/acs.iecr.9b00147.

(25) Riyajuddin, S.; Sultana, J.; Siddiqui, S. A.; Kumar, S.; Badhwar, D.; Yadav, S. S.; Goyal, S.; Venkatesan, A.; Chakraverty, S.; Ghosh, K. Silicon Nanowire–Ta2O5–NGQD Heterostructure: An Efficient Photocathode for Photoelectrochemical Hydrogen Evolution. *Sustain. Energy Fuels* **2022**, *6* (1), 197–208. https://doi.org/10.1039/D1SE01280K.

(26) Jain, A.; Ong, S. P.; Hautier, G.; Chen, W.; Richards, W. D.; Dacek, S.; Cholia, S.; Gunter, D.; Skinner, D.; Ceder, G.; Persson, K. A. Commentary: The Materials Project: A Materials Genome Approach to Accelerating Materials Innovation. *APL Mater.* **2013**, *1* (1), 11002. https://doi.org/10.1063/1.4812323.

(27) Singh, A. K.; Zhou, L.; Shinde, A.; Suram, S. K.; Montoya, J. H.; Winston, D.; Gregoire, J. M.; Persson, K. A. Electrochemical Stability of Metastable Materials. *Chem. Mater.* **2017**, *29* (23), 10159–10167. https://doi.org/10.1021/acs.chemmater.7b03980.

(28) Zhang, J.-Y.; Boyd, I. W. Thin Tantalum and Tantalum Oxide Films Grown by Pulsed Laser Deposition. *Appl. Surf. Sci.* **2000**, *168* (1), 234–238. https://doi.org/https://doi.org/10.1016/S0169-4332(00)00605-X.

(29) Wu, X. M.; Wu, P. K.; Lu, T. -M.; Rymaszewski, E. J. Reactive Sputtering Deposition of Low Temperature Tantalum Suboxide Thin Films. *Appl. Phys. Lett.* **1993**, *62* (25), 3264–3266. https://doi.org/10.1063/1.109094.

(30) Song, S. J.; Park, T.; Yoon, K. J.; Yoon, J. H.; Kwon, D. E.; Noh, W.; Lansalot-Matras, C.; Gatineau, S.; Lee, H.-K.; Gautam, S.; Cho, D.-Y.; Lee, S. W.; Hwang, C. S. Comparison of the Atomic Layer Deposition of Tantalum Oxide Thin Films Using Ta(NtBu)(NEt2)3, Ta(NtBu)(NEt2)2Cp, and H2O. *ACS Appl. Mater. Interfaces* **2017**, *9* (1), 537–547. https://doi.org/10.1021/acsami.6b11613.

(31) Denny, Y. R.; Firmansyah, T.; Oh, S. K.; Kang, H. J.; Yang, D.-S.; Heo, S.; Chung, J.; Lee, J. C. Effect of Oxygen Deficiency on Electronic Properties and Local Structure of Amorphous Tantalum Oxide Thin Films. *Mater. Res. Bull.* **2016**, *82*, 1–6. https://doi.org/https://doi.org/10.1016/j.materresbull.2016.03.004.

(32) Bondi, R. J.; Desjarlais, M. P.; Thompson, A. P.; Brennecka, G. L.; Marinella, M. J. Electrical Conductivity in Oxygen-Deficient Phases of Tantalum Pentoxide from First-Principles Calculations. *J. Appl. Phys.* **2013**, *114* (20), 203701. https://doi.org/10.1063/1.4829900.

(33) Boughaba, S.; Islam, M. U.; Sproule, G. I.; Graham, M. J. Characterization of Tantalum Oxide Films Grown by Pulsed Laser Deposition. *Surf. Coatings Technol.* **1999**, *120–121*, 757–764. https://doi.org/https://doi.org/10.1016/S0257-8972(99)00371-0.

(34) Atanassova, E.; Spassov, D. X-Ray Photoelectron Spectroscopy of Thermal Thin Ta2O5 Films on Si. *Appl. Surf. Sci.* **1998**, *135* (1), 71–82. https://doi.org/https://doi.org/10.1016/S0169-4332(98)00278-5.

(35) Atanassova, E.; Dimitrova, T.; Koprinarova, J. AES and XPS Study of Thin RF-Sputtered Ta2O5 Layers. *Appl. Surf. Sci.* **1995**, *84* (2), 193–202. https://doi.org/https://doi.org/10.1016/0169-4332(94)00538-9.

(36) Li, Y.; Sanna, S.; Norrman, K.; Christensen, D. V.; Pedersen, C. S.; Lastra, J. M. G.; Traulsen, M. L.; Esposito, V.; Pryds, N. Tuning the Stoichiometry and Electrical Properties of Tantalum Oxide Thin Films. *Appl. Surf. Sci.* **2019**, *470*, 1071–1074. https://doi.org/https://doi.org/10.1016/j.apsusc.2018.11.153.

(37) Paracchino, A.; Laporte, V.; Sivula, K.; Grätzel, M.; Thimsen, E. Highly Active Oxide Photocathode for Photoelectrochemical Water Reduction. *Nat Mater* **2011**, *10* (6), 456–

461.

(38) Kovalev, M. K.; Ren, H.; Zakir Muhamad, M.; Ager, J. W.; Lapkin, A. A. Minor Product Polymerization Causes Failure of High-Current CO2-to-Ethylene Electrolyzers. *ACS Energy Lett.* **2022**, *7* (2), 599–601. https://doi.org/10.1021/acsenergylett.1c02450.

(39) Bushuyev, O. S.; De Luna, P.; Dinh, C. T.; Tao, L.; Saur, G.; van de Lagemaat, J.; Kelley, S. O.; Sargent, E. H. What Should We Make with CO2 and How Can We Make It? *Joule* **2018**, *2* (5), 825–832. https://doi.org/https://doi.org/10.1016/j.joule.2017.09.003.

(40) Wu, Y.; Bakker, D. C. E.; Achterberg, E. P.; Silva, A. N.; Pickup, D. D.; Li, X.; Hartman, S.; Stappard, D.; Qi, D.; Tyrrell, T. Integrated Analysis of Carbon Dioxide and Oxygen Concentrations as a Quality Control of Ocean Float Data. *Commun. Earth Environ. 2022 31* **2022**, *3* (1), 1–11. https://doi.org/10.1038/s43247-022-00421-w.

(41) Barecka, M. H.; Ager, J. W.; Lapkin, A. A. Carbon Neutral Manufacturing via On-Site CO2 Recycling. *iScience* **2021**, *24* (6), 102514. https://doi.org/https://doi.org/10.1016/j.isci.2021.102514.

(42) Kawajiri, K.; Tahara, K.; Uemiya, S. Lifecycle Assessment of Critical Material Substitution: Indium Tin Oxide and Aluminum Zinc Oxide in Transparent Electrodes. *Resour. Environ. Sustain.* **2022**, *7*, 100047. https://doi.org/10.1016/J.RESENV.2022.100047.

(43) Barecka, M.; Zieminska, A.; Zbicinski, I. Towards More Sustainable TCO Layers: Environmental Effects of Replacement of ITO by Alternative Materials. *INREP Proj. Rev. http//www.inrep.eu/files/TCO%202017/INREP_TCO2017_Presentation_TUL_170921.pdf* **2017**.

(44) Statista. Tantalum price 2021 | Statista https://www.statista.com/statistics/1009173/tantalum-price/.

(45) MacroTrends. Copper Prices - 45 Year Historical Chart | MacroTrends https://www.macrotrends.net/1476/copper-prices-historical-chart-data.

(46) Tyson, M. Silicon Wafer Prices Expected to Increase by up to 25% by 2025 | Tom's Hardware https://www.tomshardware.com/news/silicon-wafer-prices-expected-to-rise-by-up-to-25-by-2025.

(47) Mayyas, A.; Ruth, M.; Pivovar, B.; Bender, G.; Wipke, K. Manufacturing Cost Analysis for Proton Exchange Membrane Water Electrolyzers https://www.nrel.gov/docs/fy10osti/72740.pdf.

(48) Barecka, M. H.; Ager, J. W.; Lapkin, A. A. Techno-Economic Assessment of Emerging CO2 Electrolysis Technologies. *STAR Protoc.* **2021**, *2* (4), 100889. https://doi.org/10.1016/J.XPRO.2021.100889.

Supporting Information:

TaO_x electron transport layers for CO_2 reduction Si photocathodes

Rajiv Ramanujam Prabhakar,[a,b,#] Raphaël Lemerle,[a,b,c,#] Magda Barecka,[d,e,f] Minki Kim,[a,b,g] Sehun Seo[a,b], Elif Nur Dayi,[a,b,c] Irene Dei Tos,[a,b] and Joel W. Ager,[a,b,h,i,]*

[a]Liquid Sunlight Alliance, Lawrence Berkeley National Laboratory, Berkeley, California 94720, United States

[b]Chemical Sciences Division, Lawrence Berkeley National Laboratory, Berkeley, California 94720, United States

[c]Materials Science and Engineering, École Polytechnique Fédéral de Lausanne, Lausanne 1015, Switzerland

[d]Department of Chemical Engineering, Northeastern University, 360 Huntington Avenue, 02215 Boston, USA; email: m.barecka@northeastern.edu

[e]Department of Chemistry and Chemical Biology, Northeastern University, 360 Huntington Avenue, 02215 Boston, USA

[f]Cambridge Centre for Advanced Research and Education in Singapore, CARES Ltd., 1 CREATE Way, CREATE Tower #05-05, 138602, Singapore.

[g]Chemical and Biomolecular Engineering, Korea Advanced Institute of Science and Technology (KAIST), Daejeon 34141, Republic of Korea

[h]Department of Materials Science and Engineering, University of California, Berkeley, Berkeley, CA 94720, USA

[i]Materials Sciences Division, Lawrence Berkeley National Laboratory, Berkeley, California 94720, United States

# These authors contributed equally

[*]jwager@lbl.gov (J. W. Ager)

Table of Contents

Silicon Substrate preparation

The Silicon wafers were cleaned by sonication in acetone (10 min), soap water (10 min), deionized water (10 min) and iso-propyl alcohol (10min) in that order. After this, they were etched to remove the native oxide layer by dipping the silicon wafers in 1% HF for 5 min. Particular emphasis was placed to make sure that immediately after the HF treatment, the wafers were either loaded into the PLD chamber or sputtering chamber to prepare the p-Silicon photocathodes. For preparation of p-Si with n^+ (phosphorus) doping - Phosphorus ions with energies of 50 keV and 30 keV and corresponding doses of $2x10^{14}$ and $1x10^{14}$ cm^{-2} were used to form the n^+ layer. The implanted wafers were then annealed at 950 °C for 30 sec in a rapid thermal annealing (RTA) furnace. n-Si photocathodes with n^+ and p^+ implants were fabricated using the procedure described elsewhere.[1]

Atomic layer deposition of TiO_2

TiO_2 was deposited by ALD onto p-Si wafers using a titanium tetraisopropoxide (TTIP) as the Ti precursor and water as the oxygen source with a thickness of 20 nm (measured by ellipsometry) at a temperature of 125°C.

Synthesis of TaO_x by pulsed laser deposition

TaO_x was deposited onto p-Si wafers using a pure Ta_2O_5 target by PLD (KrF laser 248nm) using a procedure reported in literature.[2] The PLD laser frequency was set to 10 Hz and the energy was set at 150 mJ. The oxygen flow rate during deposition was varied from 0.1 to 1.6 sccm. The deposition time was 35 mins which corresponds to a thickness of ~ 17 nm as measured by ellipsometry. During the deposition the substrate was not heated.

Synthesis of TaO_x by RF sputtering

TaO_x was deposited onto p-Si using a reactive sputtering AJA international ATC orion 5 tool equipped with a load lock chamber. A pure Ta sputtering target was used with a RF power of 150 W. The deposition pressure was 3mTorr under an atmosphere of ($Ar+O_2$). Ar to O_2 ratio was varied from 90:10, 96:4, 97:3 and 99:1. Different times of deposition was evaluated (20s to 3 min) yielding thickness of TaO_x (20 to 180 nm). The thickness was measured with a quartz crystal monitor during deposition. Only 97:3 and 99:1 yielded decent photocurrent densities and hence was pursued in depth in this work. Prior to deposition, the Ta target was presputtered for a period of 30 min to remove any oxide layer on the Ta target.

Sputtering of Cu and Au Co-catalyst

Sputtering of Cu and Au co-catalyst was performed in the same sputtering as TaO_x. Pure Cu and Au targets were used with a RF power of 100 and 150 W respectively. The deposition pressure was 3 mTorr under an Ar atmosphere. The thickness of Cu was varied from 5-20 nm and Au thickness was 5 nm (all thicknesses were measured by a quartz crystal monitor).

XPS characterization

Chemical composition of TaO_x films were obtained by XPS on a Kratos Axis Ultra DLD system at a take-off angle of 0° relative to the surface normal. An Al Kα source (hν = 1,486.6 eV) was used with a pass energy of 20 eV for the narrow scan of core levels and valence band spectra with a step size of 0.05 eV and 0.025 eV, respectively. The spectral fitting was conducted using CasaXPS analysis software.

Photoelectrochemical testing of CO_2R photocathodes

All photoelectrochemical measurements were performed using a Biologic SP-300 potentiostat under simulated AM 1.5 G illumination, calibrated using a silicon diode. Details about the polyetheretherketone (PEEK) cell employed for CO2R can be found in our prior work.[1] The PEEK cell was cleaned in nitric acid and DI water before every measurement. The working electrode (Si-TaO_x/Cu or Au) was connected to a Cu back contact with a In-Ga eutectic. The counter electrode used was a Pt wire and a leak free Ag/AgCl reference electrode was used. After the assembly of the cell, the electrolyte (0.05M K_2CO_3) was bubbled with CO_2 at a flow rate of 5 sccm and the volume of the electrolyte employed in both the cathode and anode chamber was 2 ml. Potentiostatic Electrochemical Impedance Spectroscopy (PEIS) in the dark was performed to measure the resistance of the solution. PEIS was performed from 1 MHz to 100 Hz to obtain the correct frequency in determining Rs (10 kHz). The VSP-300 potentiostat's IR compensation function only compensates 85% of Rs, thus the remaining 15% of Rs was corrected manually. Final voltage calculation after 100% IR compensation is as below:

$$V_{100\%IR_s}\ (RHE) = V_{85\%\ IR}\ (RHE) + 15\%\ \text{average}\ R_s\ (\text{Ohms}) * \text{average I (A)}.$$

Gas products characterization by gas chromatography (GC)

A SRI 8610C Gas chromatograph is used to detect and quantify the gas products. The four gas phase CO2R products (CO,CH_4,C_2H_4 and C_2H_6) and H_2 were detected and quantified using the calibration curves by injected known concentrations of gaseous products (Figure 1). Briefly in GC The CO2 was continuously flowing through the PEC cell; a portion of the exiting gas is directed into the sampling loops of the gas chromatograph. Two channels were used. Channel 1 comprises a 6' Heysep-D and a 6' Molsieve 13x column, a 1 ml sampling loop, Ar carrier gas and H2 for flame ignition. This channel is S12 equipped with a flame ionization (FID) detector and a methanizer for CO to CH4 conversion. Channel 1 has the ability to detect the CO, CH_4, C_2H_4 and C_2H_6. Channel 2 has a 6' Heysep-D column, a 2 ml sampling loop, and N_2 carrier gas. This is equipped with a TCD detector for H_2 detection

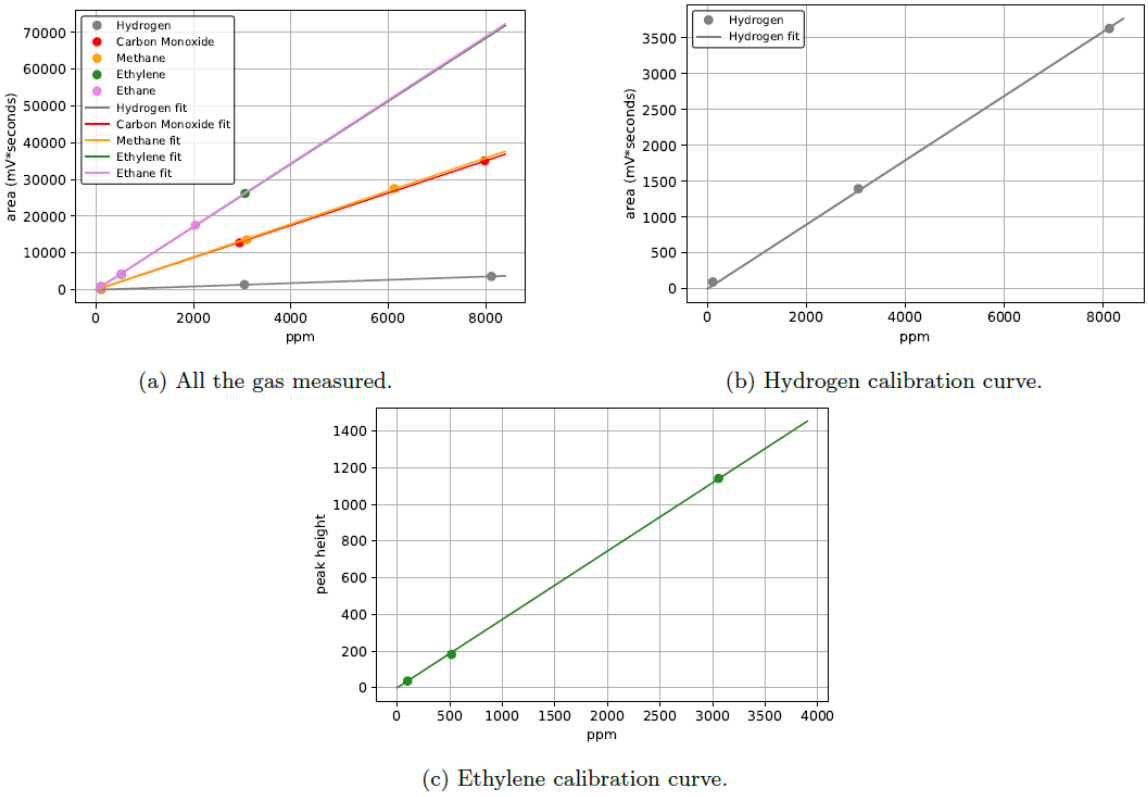

(a) All the gas measured.

(b) Hydrogen calibration curve.

(c) Ethylene calibration curve.

Figure E1. (a) Calibration curves for all the gas products measured (CO, CH_4, C_2H_4 and C_2H_6 and H_2) (b) H_2 calibration and (c) C_2H_4 calibrations for more clarity.

The Faradaic efficiency of the CO_2 reduction gaseous products is estimated using the equation below

$$FE(\%) = \frac{F \times n \times x \times F_{CO2}}{I}$$

where F is the Faraday constant (96485 C mol^{-1}), n is the number of the electrons required for a particular CO_2 reduction product, x is the mole fraction of the gaseous product obtained from the GC, F_{CO2} is the molar flow rate of CO_2 through the cell, and I is the average current during the run. The number of electrons required are 2, 8, and 12 for CO, CH_4 and C_2H_4.

Liquid products characterization by NMR

The quantification of liquid products using 1D ^1H NMR(Bruker 500 MHz) using 50 mM phenol and 10 mM dimethyl sulfoxide (DMSO) as the internal standards for quantification. The water peak was suppressed by a presaturation sequence. 400 µL of electrolyte after CO_2 photoelectrolysis was added to 50 µL of D_2O and 50 µL of internal standard solution. To determine the concentration of each CO_2R product, the area of their corresponding peak should be compared with the area of the standards. For all peaks on the left side of the water peak (> 4.7 ppm), the phenol is the calibration standard. For all peaks on the right side of the water peak (< 4.7 ppm), DMSO is the calibration standard. The product were identified using the work of marc Robert.[3] The concentration of each product $C_{product\ tube}$ in the tube can be computed using the following equation.

$$C_{product} = C_{standard\ tube} \times \frac{\frac{A_{Product}}{H_{product}}}{\frac{A_{standard}}{H_{standard}}}$$

A corresponds to the area of the peak and **H** corresponds to the number of protons corresponding to this peak. Finally, the faradaic efficiency of the liquid product can be computed using the following equation.

$$FE = \frac{C_{product} \times V_e \times n \times F}{I \times t}$$

V_E corresponds to the volume of the electrolyte; n is the number of the electrons required for a particular CO_2R product, t corresponds to the duration of the electrochemical test [s] and $C_{product}$ corresponds to the concentration of product in the electrolyte

Techno-economic analysis

Techno-economic analysis was performed deploying a recently proposed protocol for assessment of emerging electrolysis technologies (M. H. Barecka et al., 2021b). Following data was introduced to the calculation tool attached to the protocol; this dataset is derived from our experiments and the goals defined for the technology scale-up:

- Current density: 0.01 A/cm^2
- Voltage: 1.2 V
- CO_2 conversion: 75%
- Faradaic Efficiences : 20% ethylene, 2% carbon monoxide, 8% methane, 4% hydrogen,
- Electrode size : 50,000 m^2
- Market price of electrolysis product stream: 0.1 $/kg (as reported for syngas streams) (M. H. Barecka et al., 2021a)

We subsequently assessed the flow of the products obtained from such system and calculated the value as a function of the imposed CO_2 tax credit, calculated using the Equation 1. The CO_2 credit is assumed to be imposed proportionally to the stochiometric amount of CO_2 emissions resulting from combustion of produced amount of ethylene, carbon monoxide and methane. Using our method, these compounds are obtained from biogenic CO_2 thus the production method allows to avoid the emissions which would be otherwise associated petroleum-based methods.

$$Electrolysis\ stream\ value = market\ price + (88/28 \cdot ethylene\ fraction + 44/16 \cdot methane\ fraction + 44/28 \cdot carbon\ monoxide\ fraction) \quad (1)$$

To assess the investment cost into photoelectrocatalytic system, we consider all components of a large reactor that include cathode material, selemion membrane, anode material based on platinum group metal, the balance of the plant including e.g. necessary power connection and installation costs (see Supplementary Table 1 with data for Cu electrode and Supplementary Table 2 for Au electrode).

To evaluate the return on investment, the total investment into the photoelectrocatalytic system was divided by value generated yearly, which is a function of the CO_2 credit and electricity price.

The results of the sensitivity analysis for Au-based systems are given in Supplementary Figure S16.

Supplemental Figures

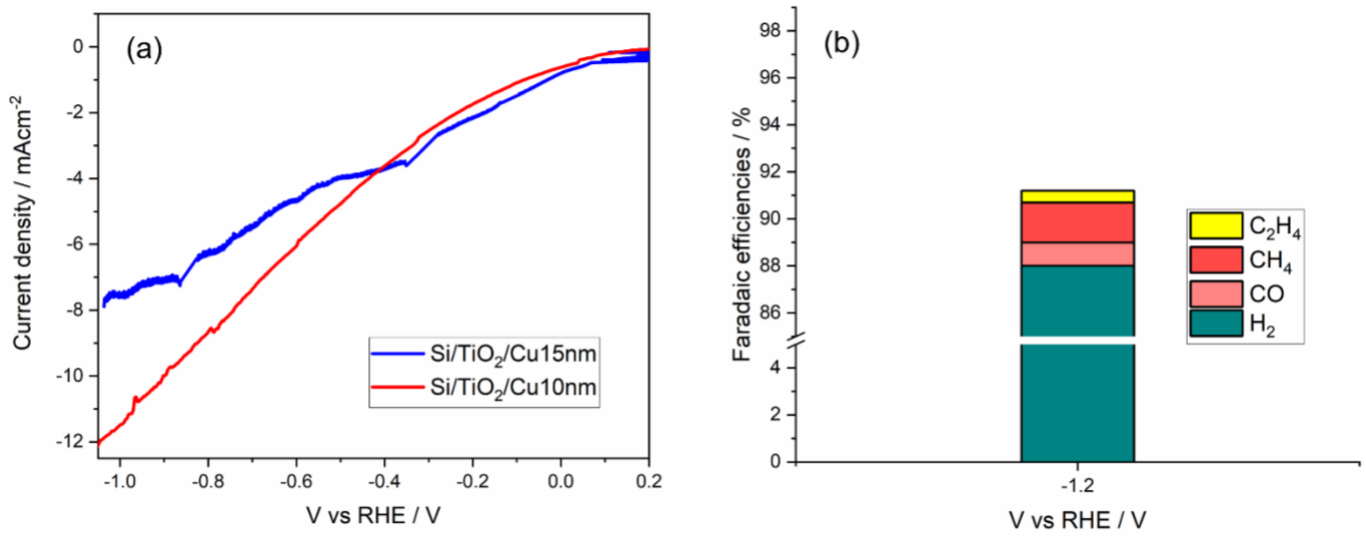

Figure S1. (a) Current density (J) vs Voltage (V) plots for $Si/TiO_2/Cu10$ nm and $Si/TiO_2/Cu15$ nm under 1 sun illumination in 0.1M $KHCO_3$ (b) Faradaic efficiencies of CO_2R products for $Si/TiO_2/Cu15$ nm under 1 sun illumination in 0.1M $KHCO_3$.

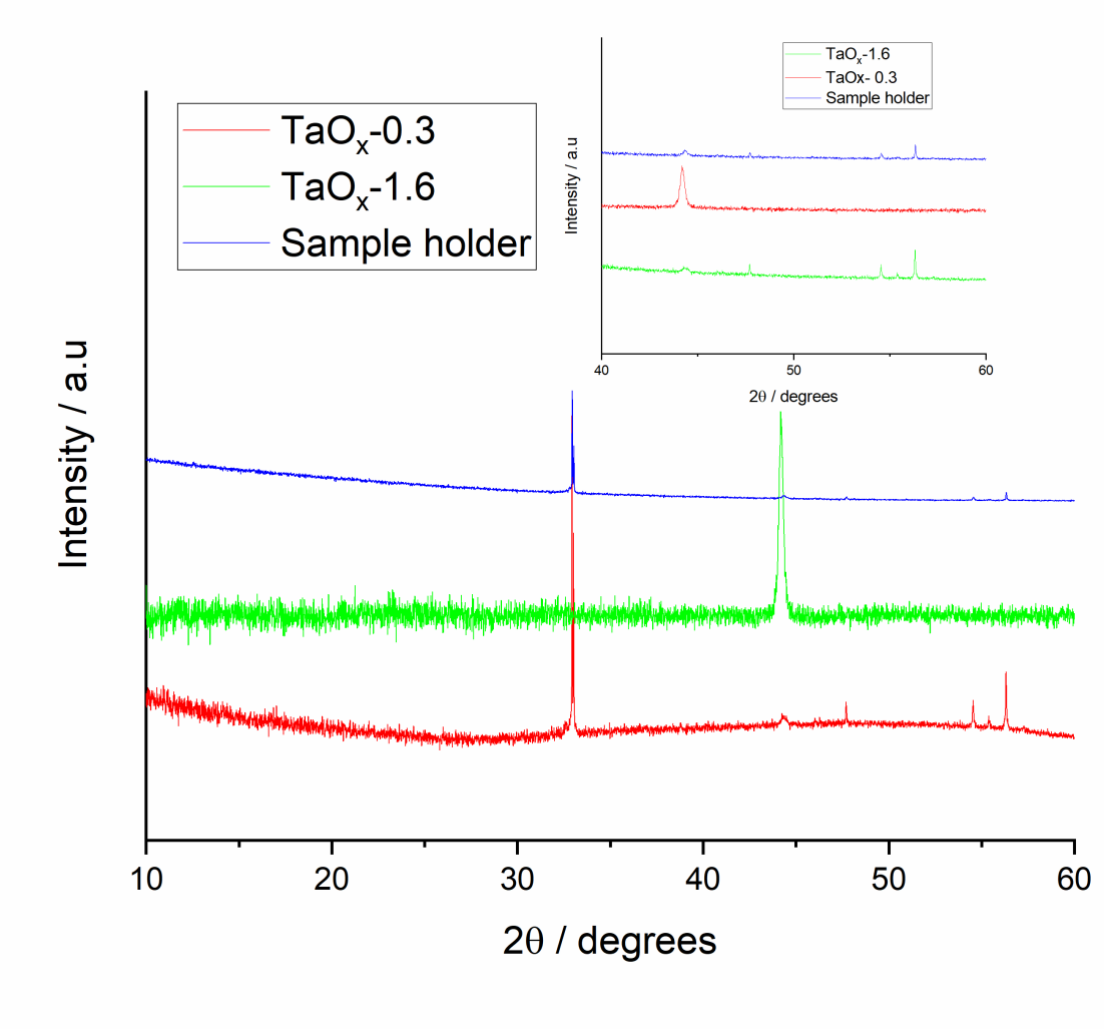

Figure S2. XRD patterns for PLD-grown TaO_x-0.3 and TaO_x-1.6 grown on glass substrates showing the amorphous nature of the PLD-grown films. The XRD peaks observed were from the sample holder of the XRD and peaks corresponding to tantalum oxide phases were not observed.

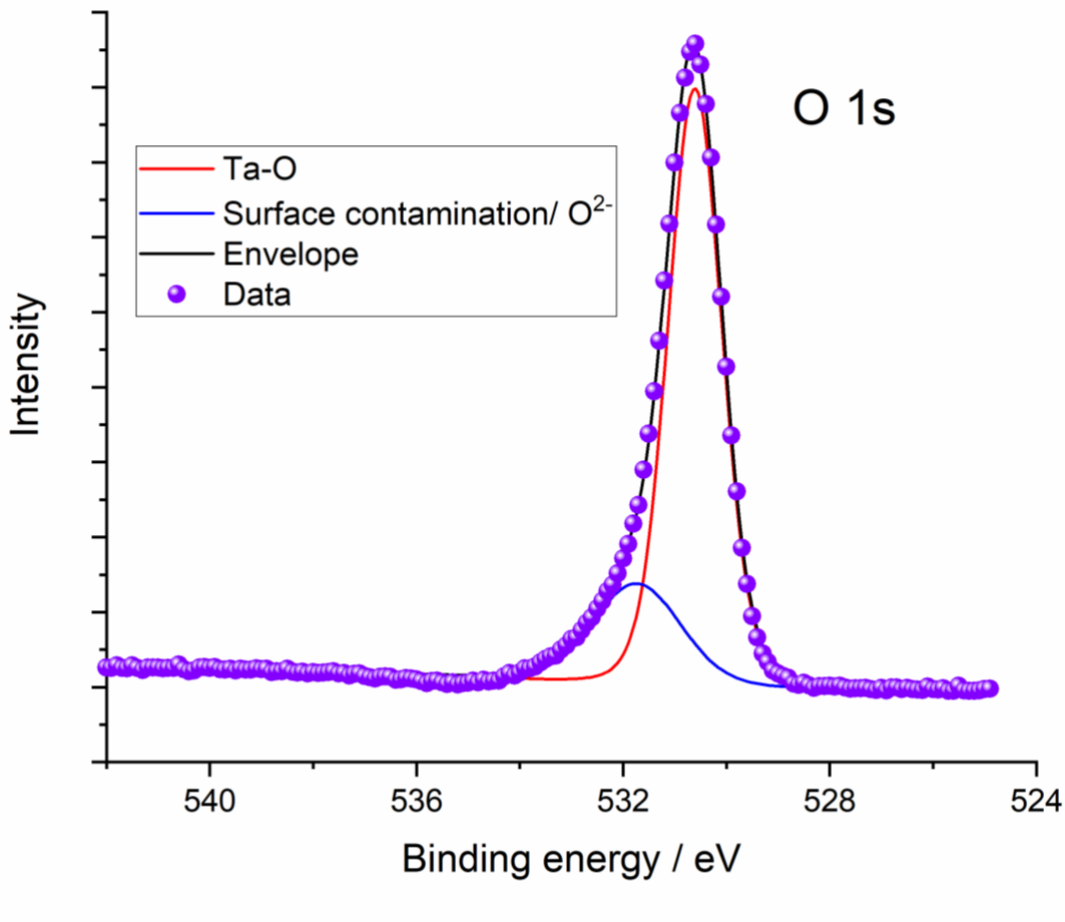

Figure S3. Core level O 1s spectrum of TaO_x-0.3 PLD grown film.

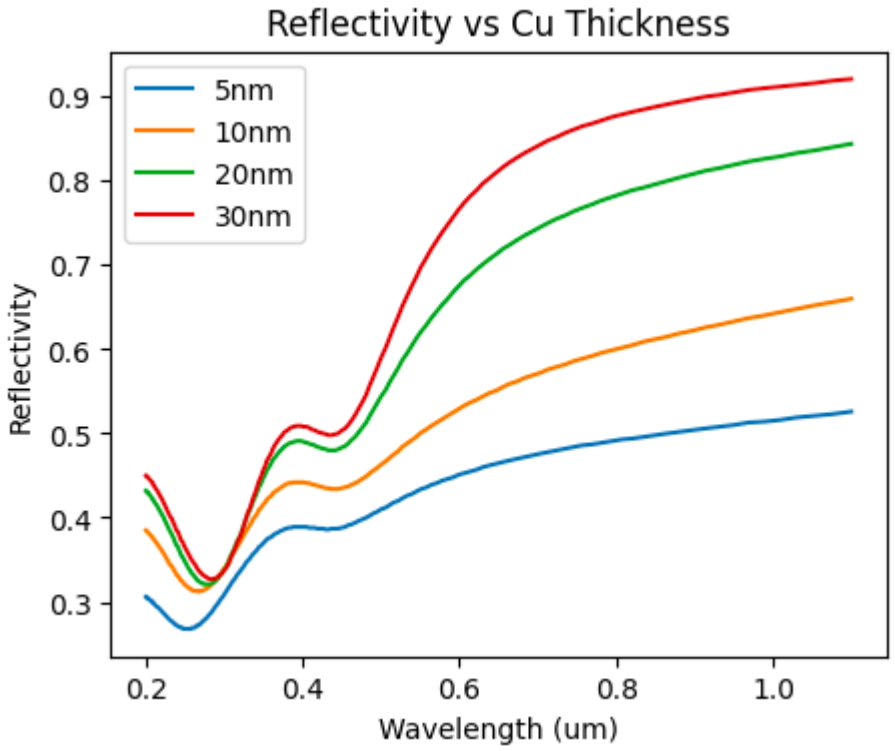

Figure S4. Finite-difference time-domain (FDTD) simulations using MEEP to estimate the reflectivity of Si/TaO_x/Cu stacks with varying Cu thickness.

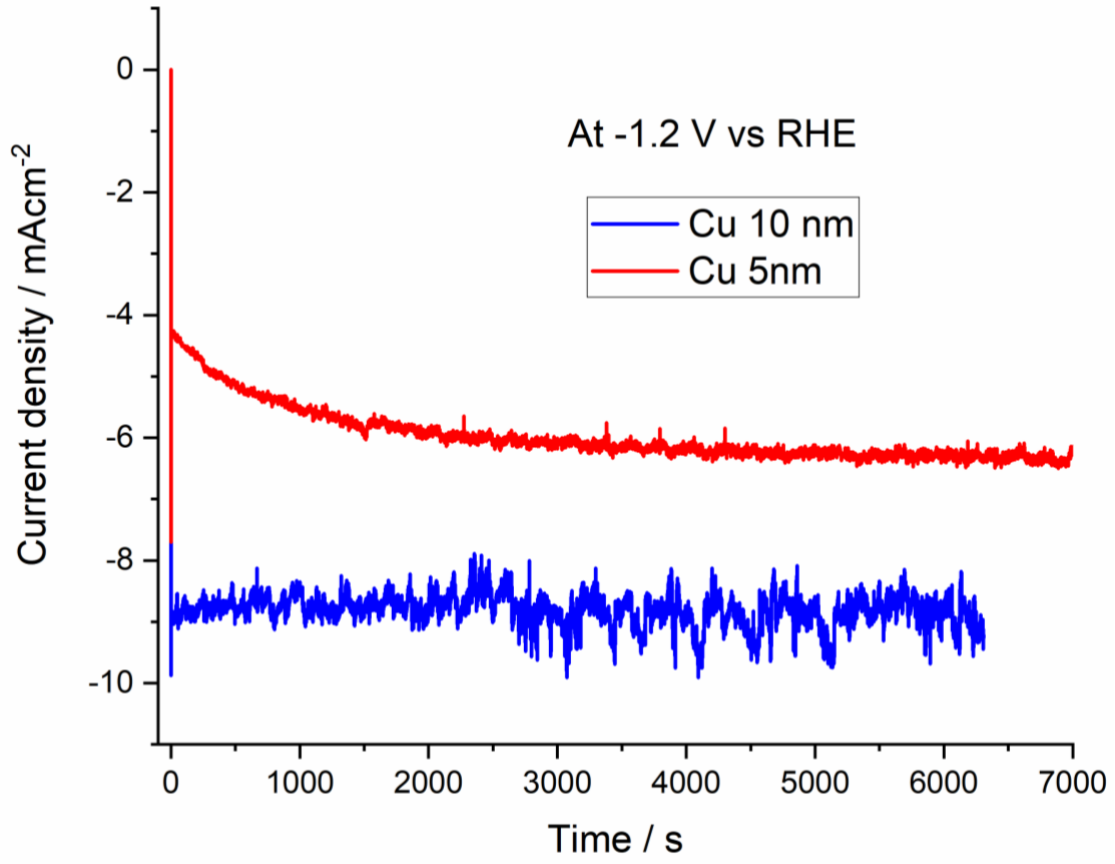

Figure S5. Current vs time plots for p-Si/TaO_x-0.3/Cu-5nm and p-Si/TaO_x-0.3/Cu-10nm at -1.2 V vs RHE under 1 sun illumination in CO_2 saturated 0.1 M $KHCO_3$ showing the lower photocurrent density observed with Cu-5nm.

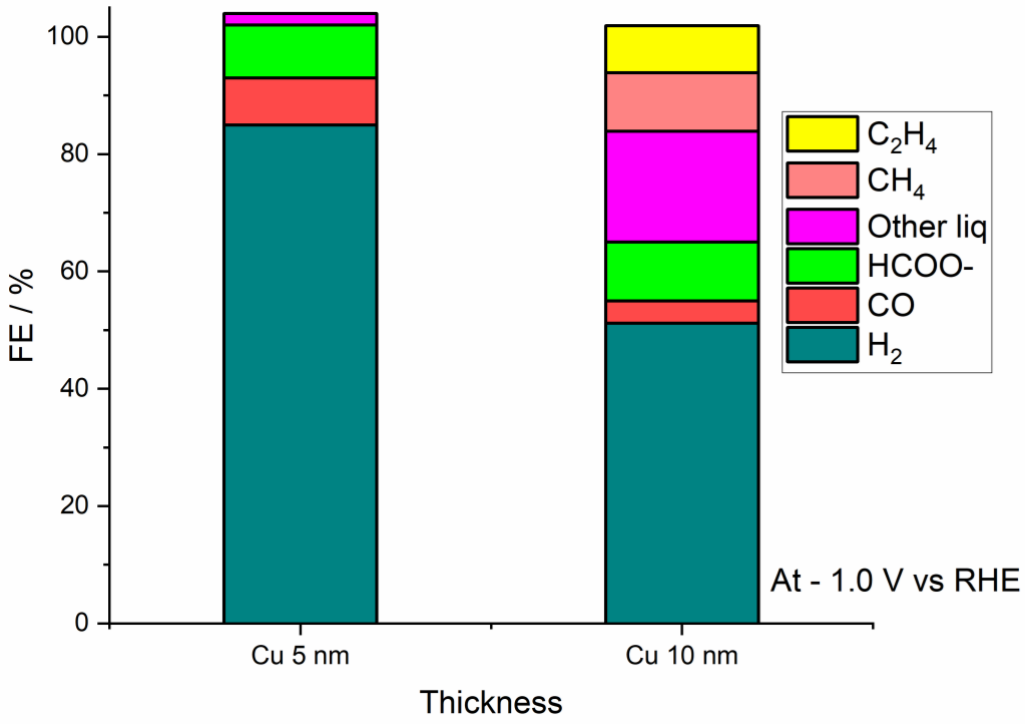

Figure S6. Comparison of the product distribution different Cu thickness at -1.0 V vs RHE for p-Si/TaO_x/Cu under 1 sun illumination in CO_2 saturated 0.1 M $KHCO_3$. More CO_2R products were observed for Cu catalyst thickness of 10 nm.

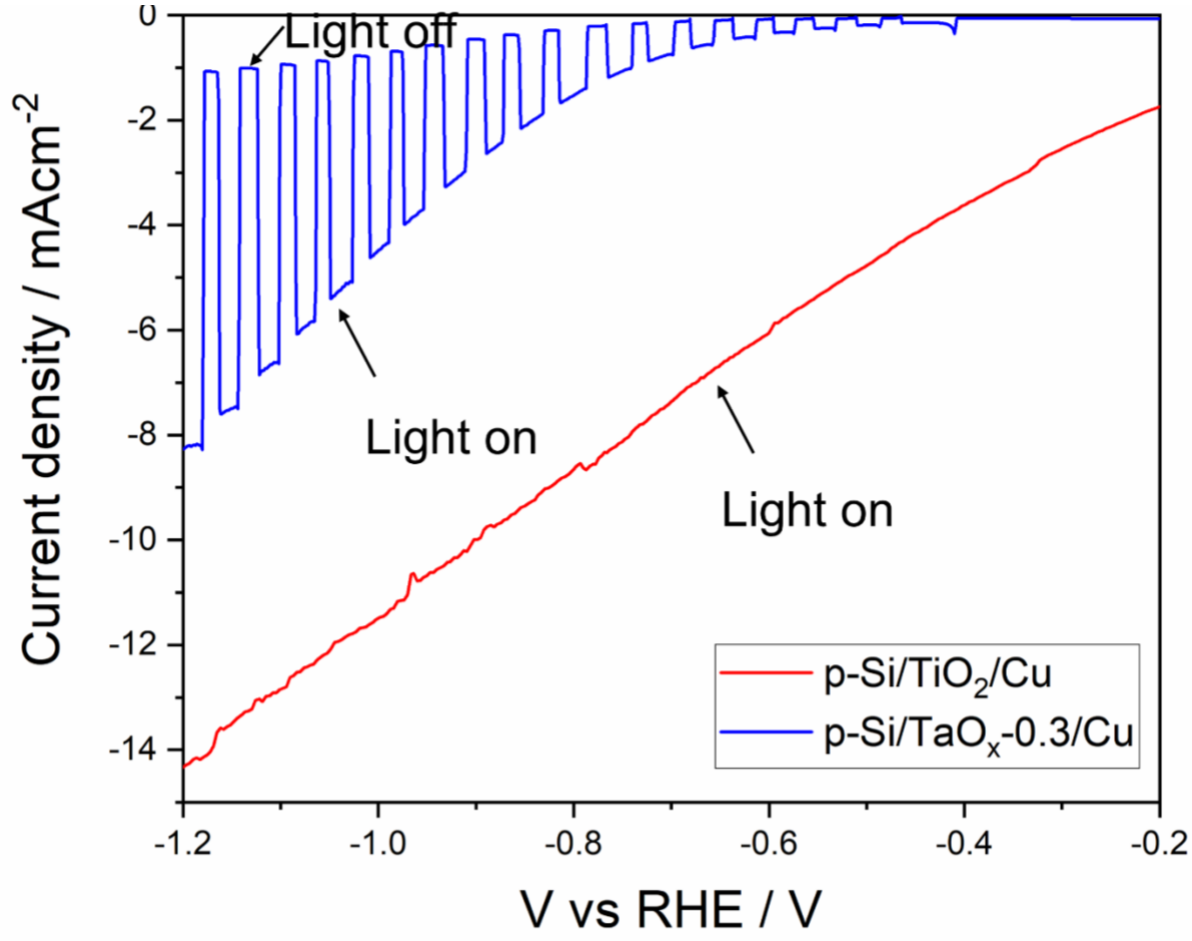

Figure S7. Comparison of current density vs Voltage plots for p-Si/TiO_2/Cu and p-Si/TaO_x-0.3/Cu showing earlier onset of photocurrent density for p-Si/TiO_2/Cu. Cu thickness of 10 nm was employed for both devices.

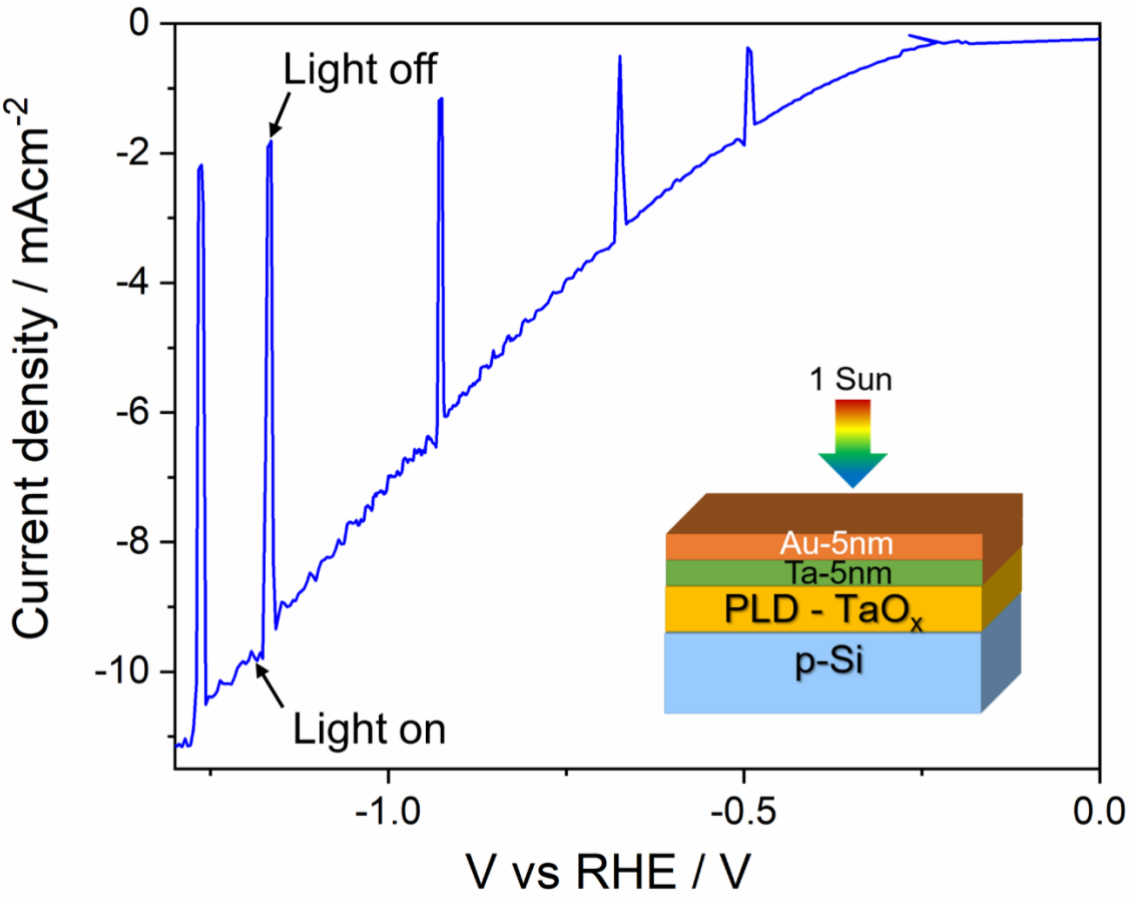

Figure S8. Current density vs Voltage plots of p-Si/TaO_x-0.3/Ta/Au photocathode under 1 sun illumination in 0.1 M $KHCO_3$.

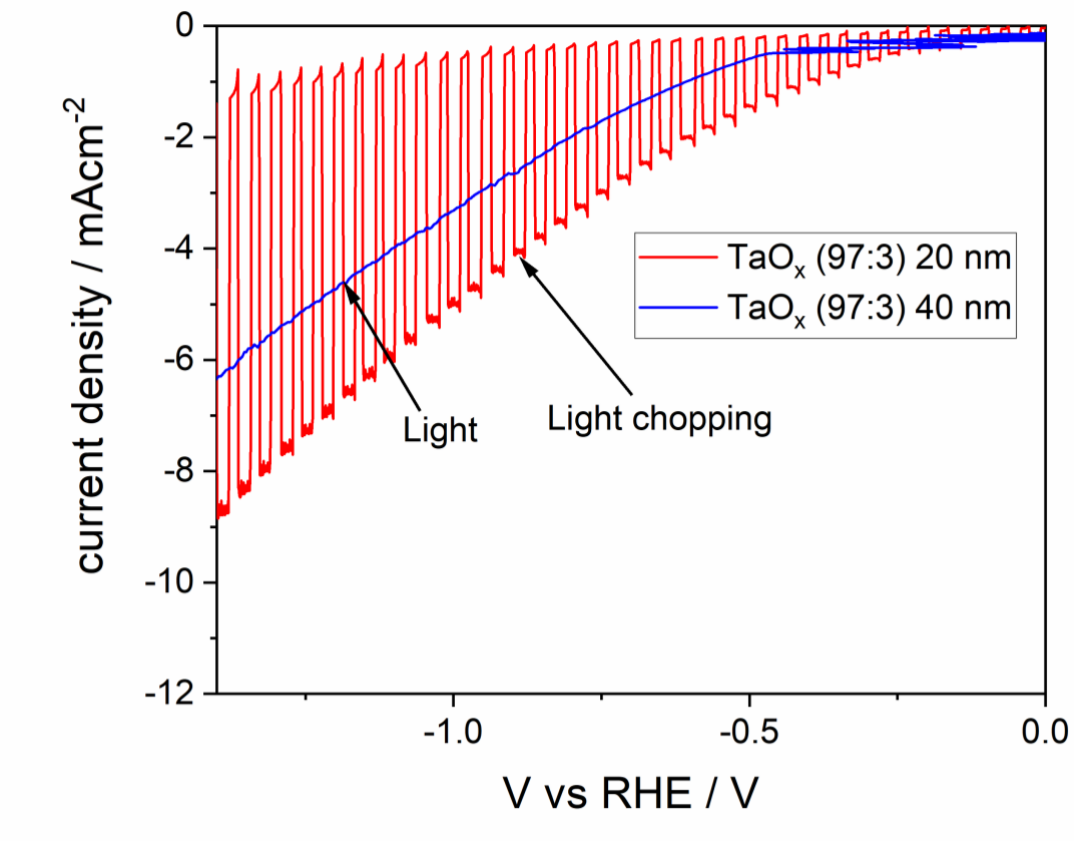

Figure S9. Comparison of Current density vs Voltage plots of p-Si/TaO_x(97:3)/Cu photocathode for 2 different thickness of the TaO_x (20 and 40 nm) under 1 sun illumination in 0.1 M $KHCO_3$ showing a later photocurrent onset and poorer fill factor for 40 nm TaO_x thickness.

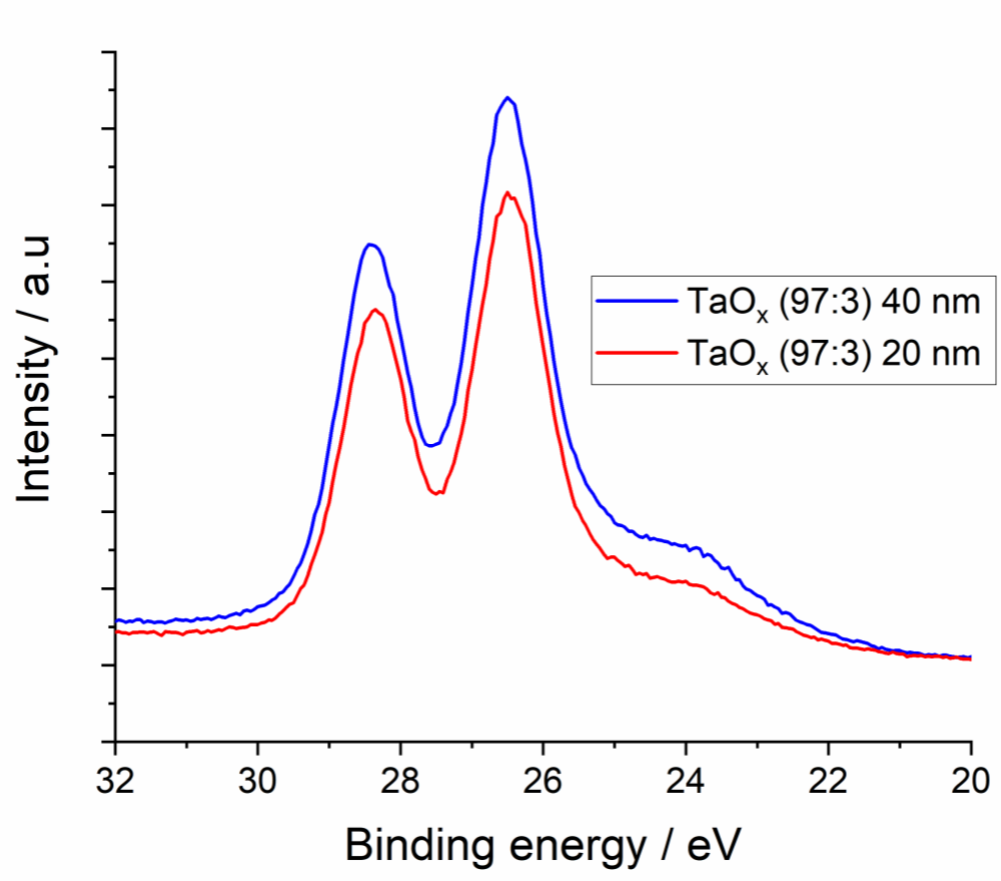

Figure S10. Ta 4f core level spectra of 20 and 40 nm thick TaO_x with an $Ar:O_2$ ratio of 97:3.

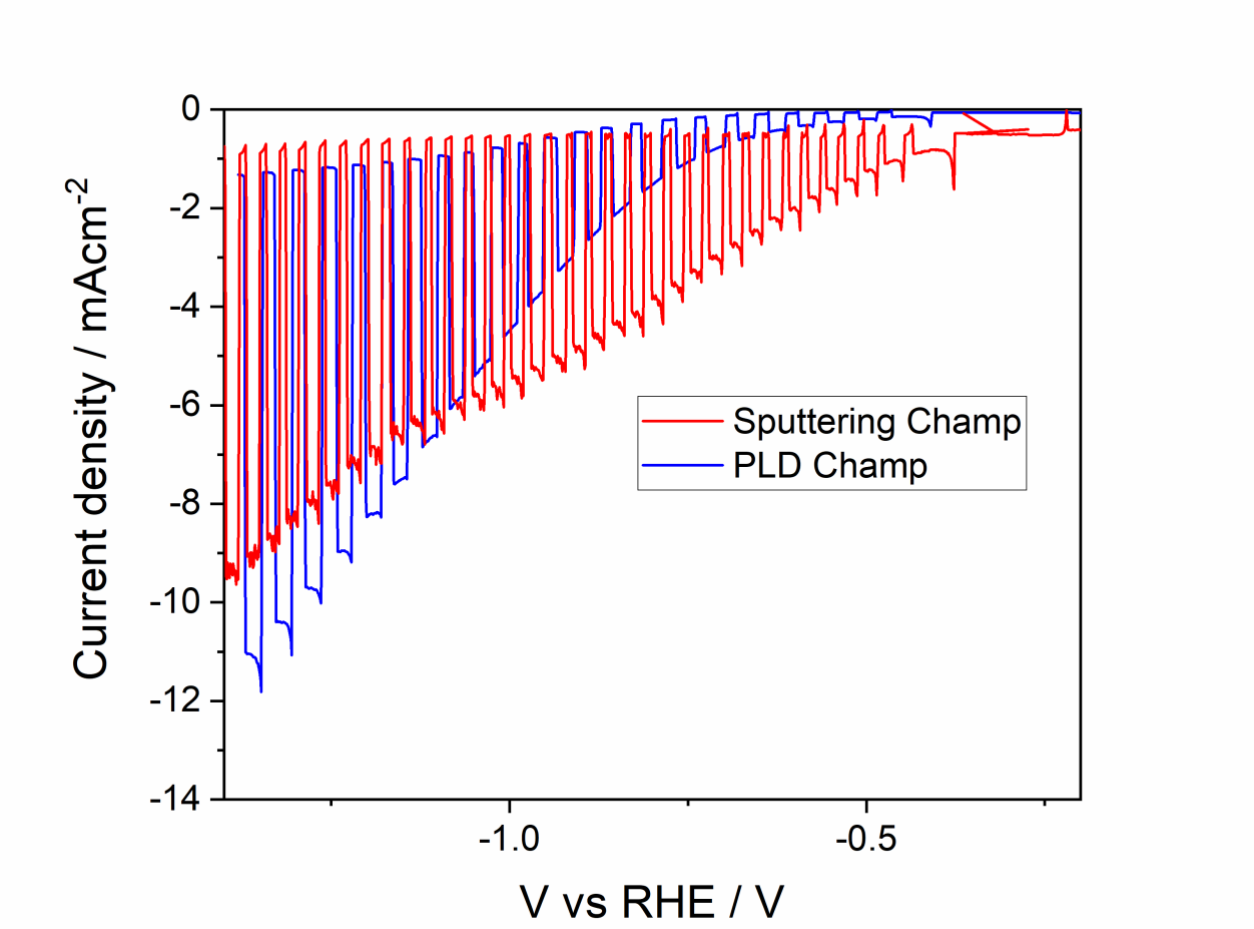

Figure S11. Comparison of the Current density vs Voltage plots for the champion (Champ) device prepared by PLD and Sputtering under 1 sun illumination in 0.1 M $KHCO_3$.

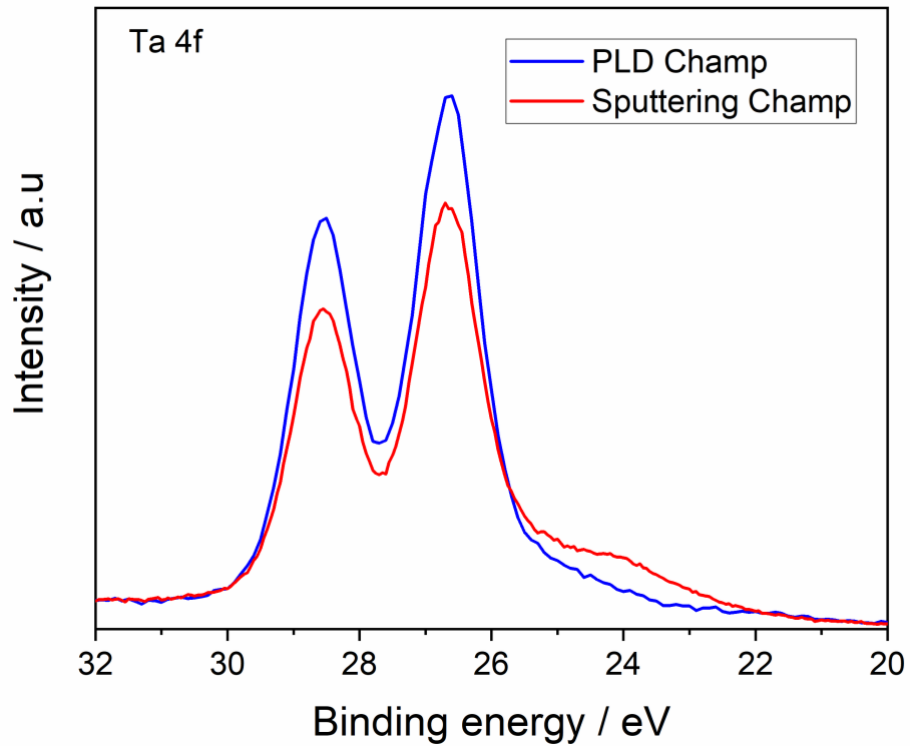

Figure S12. Comparison of Ta 4f core spectra of TaOx-0.3 prepared by PLD and TaO_x (97:3) prepared by RF sputtering which yielded the best PEC performance (champion device).

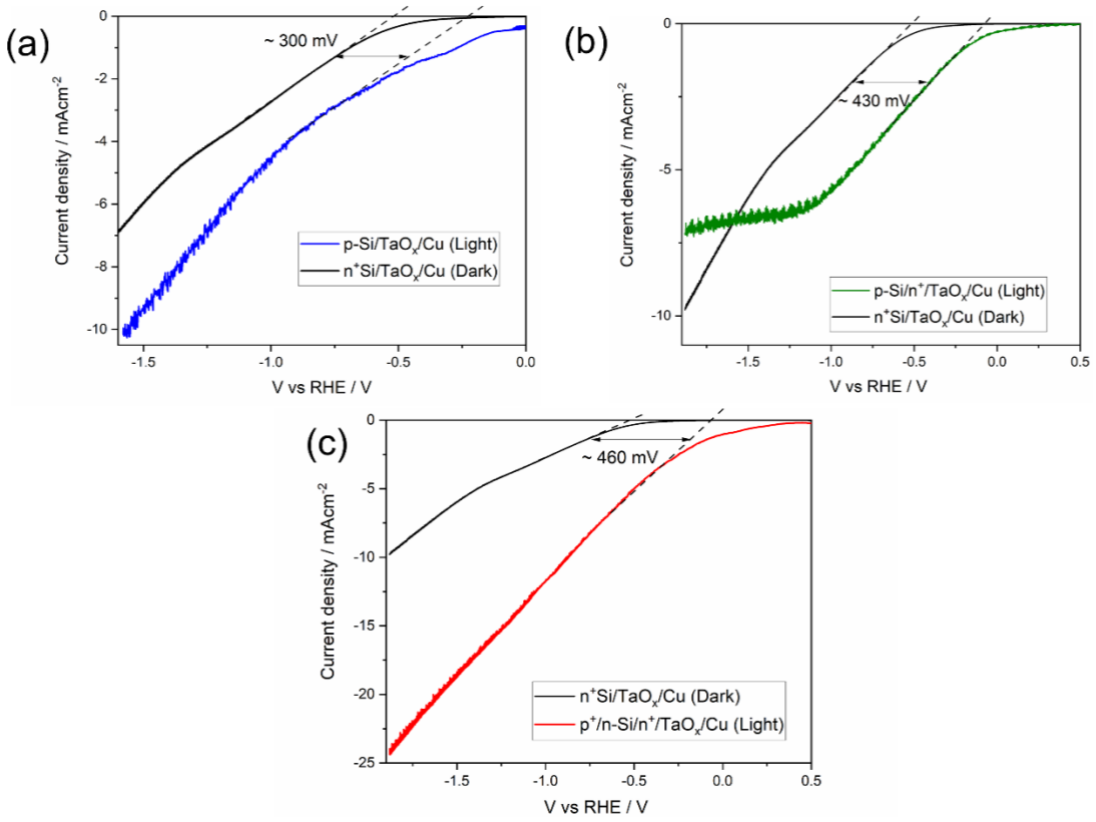

Figure S13. Estimation of photovoltage for (a) p-Si/TaO_x/Cu (b) p-Si/n^+/TaO_x/Cu (c) p^+/n-Si/n^+/TaO_x/Cu photocathode by comparing with the dark cathode of n^+Si/TaO_x/Cu.

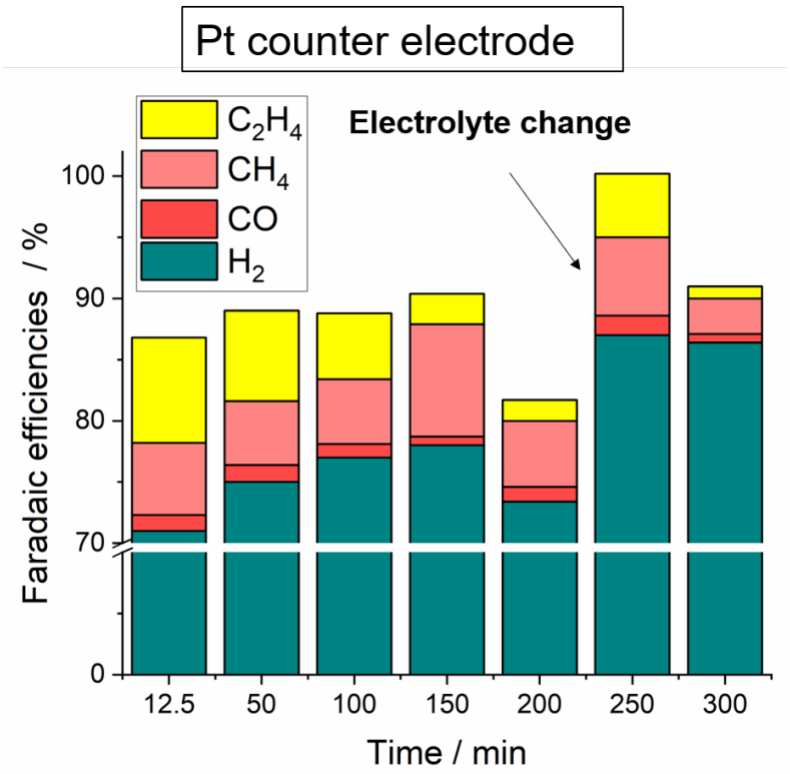

Figure S14. Gaseous CO_2R product distribution as a function of time for Si/TaO_x(97:3)/Cu10nm photocathode under 1 sun illumination in 0.1 M $KHCO_3$ at -1.2 V vs RHE with a Pt counter electrode. Electrolyte was changed after 225 mins and then C_2H_4 production increased and quickly reduced. There was also observable Pt migration from the counter electrode to the photocathode which could explain the increased HER and reduced CO_2R product evolution This has been observed in prior reports by Ren et al[4] and Gurudayal et al[1] where metal crossover from the counter electrode has resulted in increased HER activity. Given the 2 set of results from our experiments, first the reduced hydrophobicity of the surface and second the Pt migration from the counter electrode, the most likely cause for increased HER activity is the Pt migration onto the photocathode. Given the thin Cu catalyst thickness we employ ~ 10 nm, even a nanometer scale Pt migration would have a drastic effect in reducing the CO_2R catalytic activity and favoring HER.

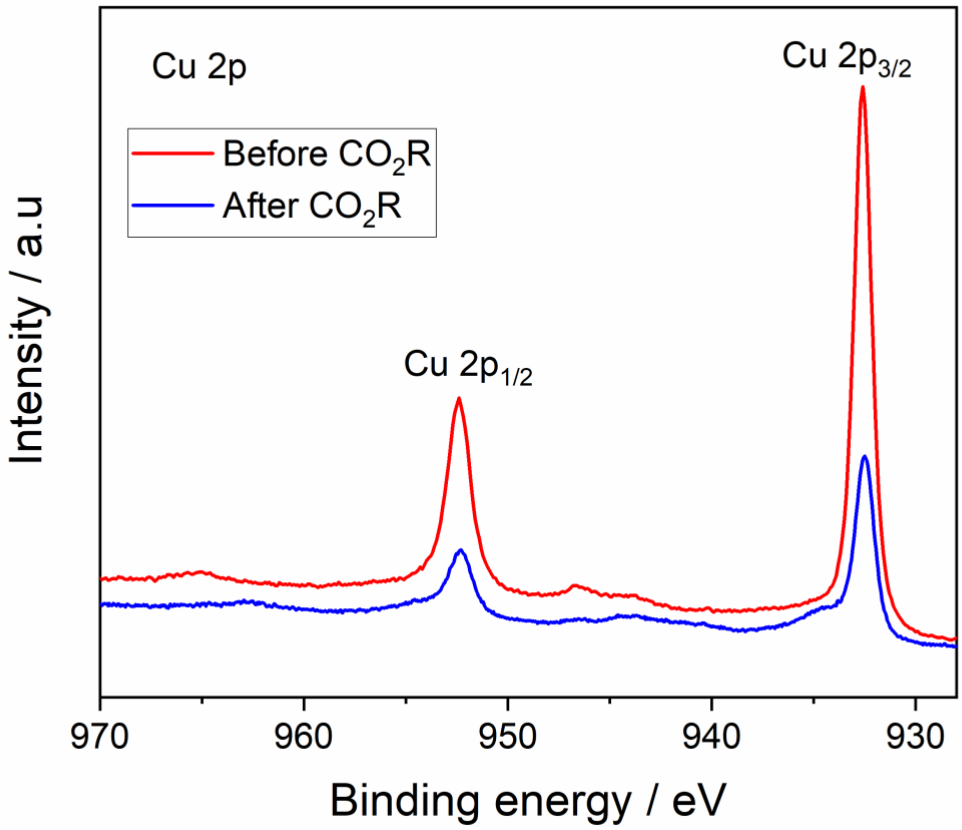

Figure S15. Cu 2p core level spectra of Si/TaO_x(97:3)/Cu before and after CO_2R operation for 300mins.

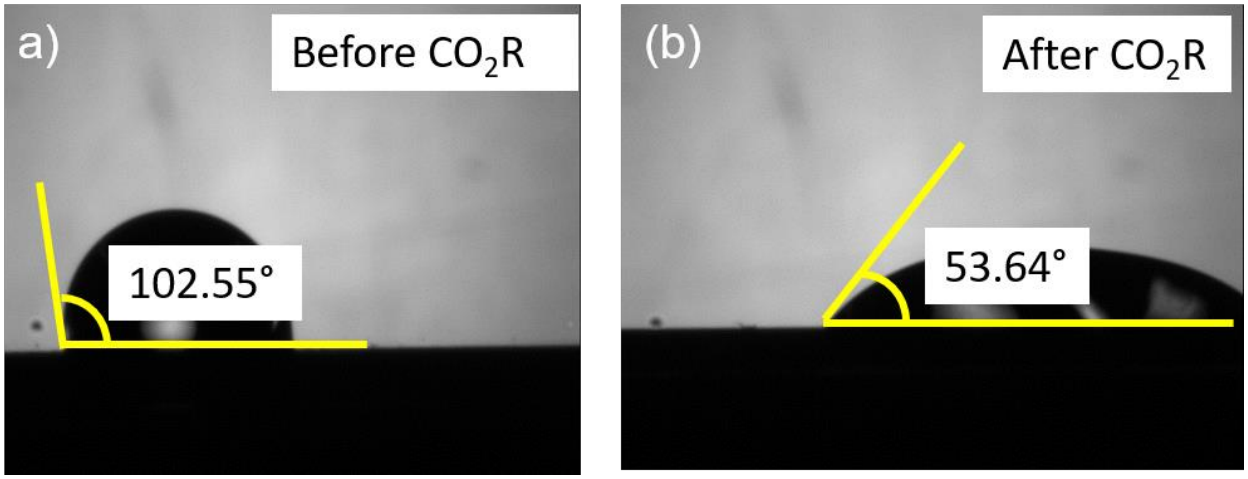

Figure S16. Contact angle measurements of p-Si/TaO_x/Cu photocathode with a Pt counter electrode during CO_2R measurements for (a) before CO_2R and (b) after CO_2R operation for 300 mins.

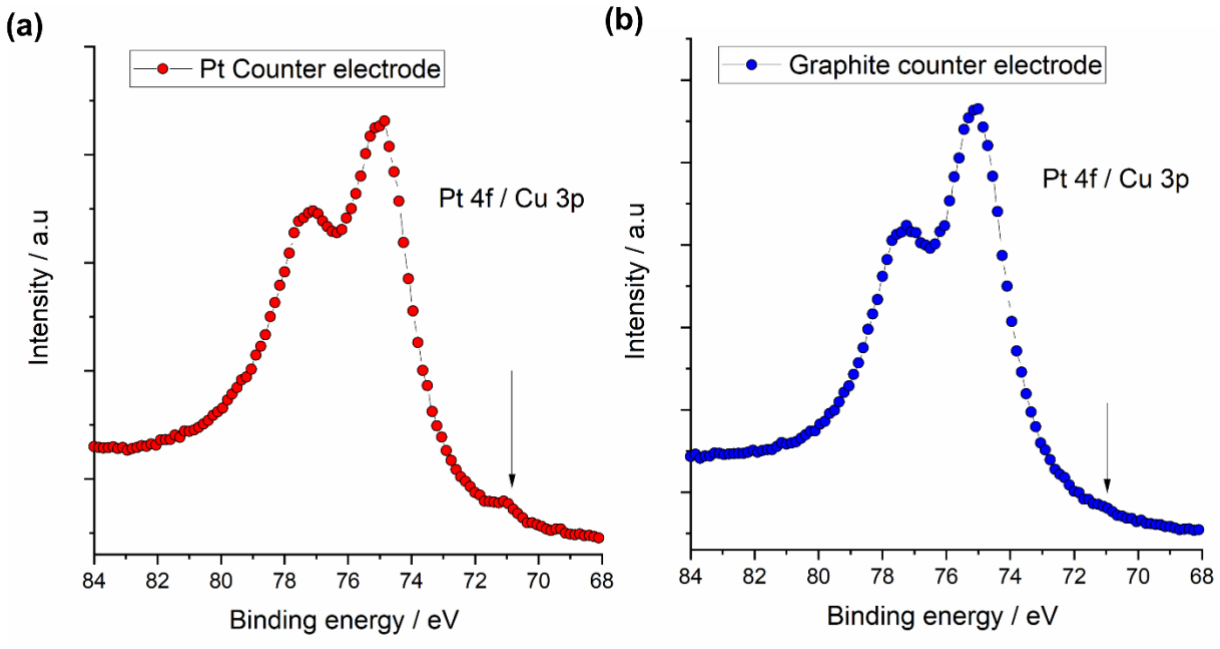

Figure S17. (a) Cu3p/Pt 4f core level spectra of Si/TaO_x (97:3)/Cu after CO_2R showing the migration of Pt from the Pt counter electrode to the photocathode (Pt 4f 71 eV). (b) Cu3p/Pt 4f core level spectra of Si/TaO_x (97:3)/Cu after CO_2R showing no Pt from the graphite counter electrode to the photocathode (Pt 4f 71 eV).[5]

Supplementary Table 1.

Input data for the assessment of the investment cost for manufacturing of **Cu-based photoelectrodes**. The cost of catalyst deposition is assessment based on pilot-plant/semi-industrial coefficients for the energy use in PVD deposition process, and the most recent price indicators for silicon, membranes, and metal cost.

Membrane cost $/m^2	500 [6]
Platinum group metal and ionomer cost $/m^2	38 [6]
Energy cost for sputtering $/m^2 (industrial benchmark: 7.53E-05 kWh/cm^2)	0.015 [7]
Argon cost $/m^2 (industrial benchmark: 1.21E-7 m^3/cm^2)	3.63E-05 [7]
Oxygen cost $/m^2 (industrial benchmark: 9.88E-10 m^3/cm^2)	8.47E-07 [7]
Silicon wafer cost $/m^2	1116 [8]
Cu cost $/m^2 for 10 nm layer	0.001 [9]
Ta_2O_5 cost $/m2 17 nm layer	0.022 [10]
Total cost $/m^2	1654.143
Balance of the plant (BoP)	1.3
Installation factor	1.2
Total cost for the designed electrolyzer ($M) 50,000 m^2	129.0

References

1 Gurudayal, J. W. Beeman, J. Bullock, H. Wang, J. Eichhorn, C. Towle, A. Javey, F. M. Toma, N. Mathews and J. W. Ager, *Energy Environ. Sci.*, 2019, **12**, 1068–1077.

2 Y. Li, S. Sanna, K. Norrman, D. V. Christensen, C. S. Pedersen, J. M. G. Lastra, M. L. Traulsen, V. Esposito and N. Pryds, *Appl. Surf. Sci.*, 2019, **470**, 1071–1074.

3 T. Chatterjee, E. Boutin and M. Robert, *Dalt. Trans.*, 2020, **49**, 4257–4265.

4 D. Ren, N. W. X. Loo, L. Gong and B. S. Yeo, *ACS Sustain. Chem. Eng.*, 2017, **5**, 9191–9199.

5 I. Roh, S. Yu, C.-K. Lin, S. Louisia, S. Cestellos-Blanco and P. Yang, *J. Am. Chem. Soc.*, 2022, **144**, 8002–8006.

6 A. Mayyas, M. Ruth, B. Pivovar, G. Bender and K. Wipke, Manufacturing Cost Analysis for Proton Exchange Membrane Water Electrolyzers, https://www.nrel.gov/docs/fy10osti/72740.pdf.

7 M. Barecka, A. Zieminska and I. Zbicinski, *INREP Proj. Rev. http//www.inrep.eu/files/TCO%202017/INREP_TCO2017_Presentation_TUL_170921.pdf*.

8 M. Tyson, Silicon Wafer Prices Expected to Increase by up to 25% by 2025 | Tom's Hardware, https://www.tomshardware.com/news/silicon-wafer-prices-expected-to-rise-by-up-to-25-by-2025.

9 MacroTrends, Copper Prices - 45 Year Historical Chart | MacroTrends, https://www.macrotrends.net/1476/copper-prices-historical-chart-data.

10 Statista, Tantalum price 2021 | Statista, https://www.statista.com/statistics/1009173/tantalum-price/.